EB3-informed dynamics of the microtubule stabilizing cap during stalled growth

Maurits Kok[a], Florian Huber[a,b,c], Svenja-Marei Kalisch[a], and Marileen Dogterom[a]*

a Department of Bionanoscience, Kavli Institute of Nanoscience, Faculty of Applied Sciences,

Delft Institute of Technology, van der Maasweg 9, 2629 HZ Delft, The Netherlands

b Netherlands eScience Center, Science Park 140, 1098XG Amsterdam, The Netherlands

c present affiliation: Center for Digitalization and Digitality, HSD – University of Applied

Sciences, Münsterstraße 156, 40476 Düsseldorf, Germany

* Correspondence to: Marileen Dogterom (m.dogterom@tudelft.nl, +31 (0)15 278 5937)

Key words

microtubules, EB3, dynamic instability, *in vitro* reconstitution, 1D model, microfabricated barriers, Monte Carlo simulation

16 **ABSTRACT**

17   Microtubule stability is known to be governed by a stabilizing GTP/GDP-Pi cap, but the exact

18   relation between growth velocity, GTP hydrolysis and catastrophes remains unclear. We

19   investigate the dynamics of the stabilizing cap through *in vitro* reconstitution of microtubule

20   dynamics in contact with micro-fabricated barriers, using the plus-end binding protein GFP-

21   EB3 as a marker for the nucleotide state of the tip. The interaction of growing microtubules

22   with steric objects is known to slow down microtubule growth and accelerate catastrophes. We

23   show that the lifetime distributions of stalled microtubules, as well as the corresponding lifetime

24   distributions of freely growing microtubules, can be fully described with a simple

25   phenomenological 1D model based on noisy microtubule growth and a single EB3-dependent

26   hydrolysis rate. This same model is furthermore capable of explaining both the previously

27   reported mild catastrophe dependence on microtubule growth rates and the catastrophe statistics

28   during tubulin washout experiments.

2

INTRODUCTION

Microtubules are hollow cylindrical polymers consisting of αβ-tubulin dimers arranged in a head-to-tail fashion to form protofilaments, ~13 of which typically constitute the microtubule lattice (Debs et al., 2020; Tilney et al., 1973; Zhang et al., 2015). Individual microtubules constantly switch between phases of growth and shrinkage, a fundamental process known as dynamic instability (Mitchison and Kirschner, 1984). As a major constituent of the eukaryotic cytoskeleton, microtubules are involved in many essential processes within the cell, including intracellular transport, cell division, and cell morphology (Akhmanova and Steinmetz, 2015). During these processes, dynamic microtubule ends interact with other cellular components, either through intermediary protein complexes or through direct physical contact (Colin et al., 2018; Dogterom and Koenderink, 2019; Gurel et al., 2014; Nguyen-Ngoc et al., 2007; Preciado Lopez et al., 2014; Waterman-Storer et al., 1995). Such contacts typically affect the dynamic behaviour of microtubule ends which is integral to the biological function of these interactions (Bouchet et al., 2016; Brangwynne et al., 2006; Gregoretti et al., 2006; Komarova et al., 2002; Letort et al., 2016; Tischer et al., 2009; Vleugel et al., 2016).

The biochemical mechanism behind the stochastic transition from growth to shrinkage, known as a catastrophe, is related to the progressive hydrolysis of GTP bound to β-tubulin (Carlier and Pantaloni, 1982; Nogales, 1999). During polymerization, the microtubule tip is highly dynamic due to continuous addition and removal of tubulin dimers (Gardner et al., 2011a; Kerssemakers et al., 2006; Rickman et al., 2017; Schek et al., 2007). After GTP-bound tubulin is incorporated at the microtubule tip, hydrolysis of the nucleotide followed by Pi release is hypothesized to lead to a destabilization of the lattice by a compaction around the exchangeable nucleotide (Alushin et al., 2014; Zhang et al., 2015). The delay between tubulin incorporation and hydrolysis results in a GTP/GDP-Pi enriched region at the microtubule tip, which gives rise to what is known as the stabilizing cap (Carlier and Pantaloni, 1981). Upon the loss of the stabilizing cap, a catastrophe follows upon which the strain build-up in the lattice is released during depolymerization. However, whereas this basic description of the biochemistry behind dynamic instability is generally accepted, the exact relation between GTP hydrolysis, the size of the stabilizing cap, the details of microtubule growth and the statistics of catastrophes is still not fully understood, despite the availability of a wealth of quantitative data on catastrophe statistics under different conditions (Brouhard and Rice, 2018; Ohi and Zanic, 2016).

61   Various estimates of the stabilizing cap size have been reported, from short caps of a

62   few terminal tubulin layers (Brun et al., 2009; Caplow and Shanks, 1996; Drechsel and

63   Kirschner, 1994; Karr and Purich, 1978; Walker et al., 1991) to longer caps spanning up to

64   dozens of layers (Carlier and Pantaloni, 1981; Seetapun et al., 2012). In recent years, direct

65   visualisation of the tubulin nucleotide state has become possible with the family of end binding

66   proteins (EBs) that can autonomously bind to the GDP-Pi region at the microtubule tip (Maurer

67   et al., 2011). It has been shown that the size of the EB comet at the tip correlates with the size

68   of the stabilizing cap and consequently with microtubule stability (Duellberg et al., 2016a;

69   Seetapun et al., 2012; Zhang et al., 2015). In fact, tubulin washout experiments using Mal3 (the

70   EB1 homolog in yeast) suggest that not the size of the total EB binding region is decisive in

71   preventing a catastrophe, but the presence of a critical number of unhydrolyzed subunits at the

72   terminal ~10 tubulin layers at the microtubule tip (~130 dimers) (Duellberg et al., 2016a).

73

74   Here we use the ability of EB3 to report on the status of the stabilizing cap to investigate the

75   detailed relation between cap dynamics and catastrophe statistics for stalling microtubules that

76   are pushing against microfabricated barriers. A stalling microtubule exerts a pushing force that

77   is too small to overcome its critical buckling force, resulting in the blocking of further

78   microtubule growth. The stability of pushing microtubules has previously been studied for

79   buckling and bending microtubules *in vitro* (Janson et al., 2003), *in vivo* (Brangwynne et al.,

80   2007; Odde et al., 1999; Pallavicini et al., 2017), and *in silico* (Das et al., 2014; Valiyakath and

81   Gopalakrishnan, 2018). It was established that microtubules generating pushing forces against

82   rigid barriers *in vitro* experience an increased catastrophe frequency (Janson et al., 2003; Laan

83   et al., 2008). This force-induced catastrophe is thought to be the result of a reduction in the

84   addition of tubulin dimers as the microtubule growth velocity is slowed with increasing force

85   (Janson et al., 2003; Kerssemakers et al., 2006). However, exactly how the reduction of tubulin

86   addition in combination with nucleotide hydrolysis affects the dynamics of the stabilizing cap,

87   and thereby determines the lifetime statistics for stalled microtubules, has remained unresolved.

88   We determine the lifetime statistics of stalling microtubules *in vitro* by growing

89   microtubules against micro-fabricated barriers using GFP-EB3 as a proxy for the size of the

90   stabilizing cap. By introducing a novel barrier design with a long overhang, we ensure that

91   microtubule stalling can be imaged simultaneously with the EB3 signal using TIRF microscopy.

92   We observe that microtubule stalling increases the catastrophe frequency in the absence of EB3

4

93   as previously reported (Janson et al., 2003). In the presence of EB3 the microtubule lifetime is

94   further reduced in a concentration dependent manner. Surprisingly, the full decay of the EB3

95   comet during microtubule stalling does not necessarily lead to an immediate catastrophe. We

96   compare our results to similar data obtained for freely growing microtubules under the same

97   conditions, and then perform simulations of microtubule dynamics based on a simple model in

98   an attempt to simultaneously explain both data sets.

99   Over the years, different types of models have been proposed to gain a better

100   understanding of what triggers a catastrophe. Biochemical models rely on the hydrolysis of

101   tubulin dimers to reduce the size of the stabilizing cap to trigger a catastrophe (Bayley et al.,

102   1989; Brun et al., 2009; Chen and Hill, 1985; Gardner et al., 2011a; Margolin et al., 2012;

103   Padinhateeri et al., 2012; Piedra et al., 2016; VanBuren et al., 2002). However, only with the

104   introduction of lateral interactions between dimers in a 2D model can these models capture

105   observed growth fluctuations (Gardner et al., 2011a) and observed microtubule lifetimes

106   (Bowne-Anderson et al., 2013; Lee and Terentjev, 2019). Mechanochemical models

107   additionally include the build-up of strain in the lattice and protofilament bending at the tip

108   (Bollinger and Stevens, 2019; Coombes et al., 2013; McIntosh et al., 2018; Michaels et al.,

109   2020; Molodtsov et al., 2005; VanBuren et al., 2005; Zakharov et al., 2015). Both types of

110   models can explain a variety of experimental observations of dynamic instability, but they

111   typically require many fitting parameters and do not explicitly include the highly dynamic

112   nature of the microtubule tip. Alternatively, simple phenomenological models have been useful

113   in obtaining an intuitive insight into the principles behind microtubule dynamics and the effect

114   of microtubule associated proteins (Brun et al., 2009; Duellberg et al., 2016a; Flyvbjerg et al.,

115   1996; Rickman et al., 2017).

116   To find a minimal model capable of explaining microtubule catastrophe statistics with

117   the smallest possible number of fitting parameters, we use coarse-grained Monte Carlo

118   simulations of 1D filaments (Flyvbjerg et al., 1996; Margolin et al., 2006; Padinhateeri et al.,

119   2012; Rickman et al., 2017). We show that the lifetimes of both freely growing and stalled

120   microtubules can be explained by a combination of random GTP hydrolysis and a parameter

121   that characterises the noisiness of microtubule growth, a concept that was generally missing

122   from previous phenomenological models in the description of microtubule lifetimes. We

123   confirm that while the EB binding region is a measure for the size of the stabilizing cap, there

124   is no one-to-one correlation between its presence and the onset of a catastrophe. Instead, the

125   data are consistent with a catastrophe being triggered when a large enough sequence of GDP-

5

126   bound tubulin dimers becomes exposed at the microtubule tip. Importantly, this 1D biochemical

127   model can also successfully capture the previously reported catastrophe dependence on tubulin

128   concentration, taking into account previously reported velocity-dependent growth fluctuations,

129   and it is in good agreement with previously reported catastrophe delays after tubulin dilution.

130   The so-called "ageing" of microtubules, referring to the observed increase of the catastrophe

131   frequency with microtubule age (Coombes et al., 2013; Duellberg et al., 2016b; Gardner et al.,

132   2011b; Odde et al., 1995), is not a feature of our simple model, but this behaviour naturally

133   emerges by additionally assuming that microtubule growth fluctuations increase with
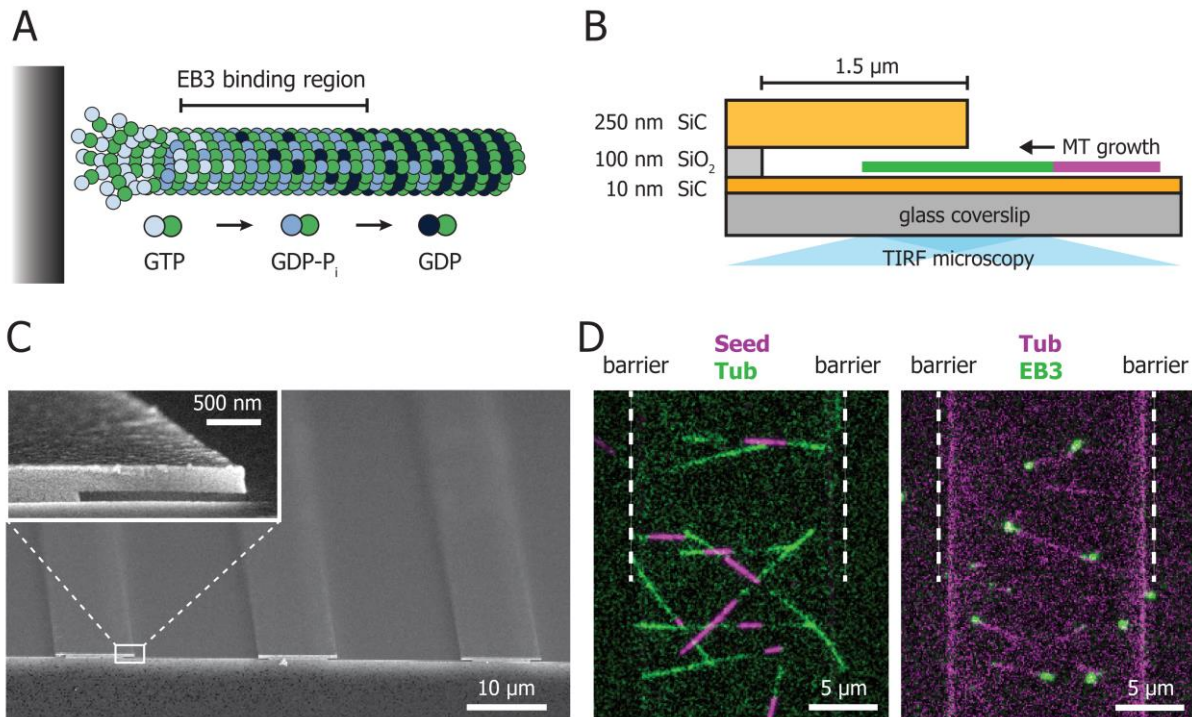
134   microtubule age.

135

136 **RESULTS**

137 *In vitro* **reconstitution of microtubule stalling**

138 To investigate the stability of stalling microtubules in the presence of different concentrations

139 of GFP-EB3, we analysed the dynamics of microtubules growing against micro-fabricated

140 barriers using an *in vitro* reconstitution assay (Bieling et al., 2007; Kalisch et al., 2011). We

141 assume each microtubule to consist of three regions: 1) a GTP rich terminal region where

142 protofilament growth takes place (Maurer et al., 2014; McIntosh et al., 2018), 2) a region

143 containing the intermediate GDP-Pi state to which EB3 preferably binds (Maurer et al., 2011),

144 and 3) the GDP lattice (Fig. 1A). The presence of EB3 is known to increase both the GTP

145 hydrolysis rate and the microtubule growth velocity by respectively compacting the

146 microtubule lattice and closing the lattice seam (Maurer et al., 2014; Zhang et al., 2015).

147 Microtubules were nucleated from GMPCPP-stabilized seeds and imaged with Total Internal

148 Reflection Fluorescence (TIRF) microscopy. The barriers were composed of 100 nm SiO_2

149 deposited on a glass coverslip with an amorphous silicon carbide (SiC) overhang,

150 approximately 1.5 μm long, to trap the microtubules and force them to grow into the barriers

151 (Fig. 1BC). SiC is a mechanically stable, optically transparent material (wavelengths > 0.5 μm)

152 with similar passivation and functionalization properties as SiO_2 due to a very thin native oxide

153 layer on its surface (Coletti et al., 2007; Dhar et al., 2009). Although fabrication of the barriers

154 requires a thin 10 nm layer of SiC on the glass surface (see Methods for details), microtubules

155 can be imaged successfully with TIRF microscopy (Fig. 1D and S1). This novel barrier design

156 enables high resolution imaging with TIRF microscopy as the microtubules are forced to remain

157 within 100 nm from the surface during barrier contact, eliminating fluctuations perpendicular

158 to the surface. The width between two barriers is 15 μm, chosen to keep the microtubules short

159 and thereby reduce the probability of observing slipping and buckling events (Janson et al.,

160 2003). All experiments were performed in the presence of 15 μM tubulin, and 0, 20, 50, or 100

161 nM GFP-EB3.

162

163 **Figure 1. *In vitro* reconstitution of microtubule stalling. (A)** Schematic depiction of the nucleotide distribution at the

164 microtubule tip. Progressive hydrolysis of GTP-tubulin after incorporation leads to a destabilized lattice that is stabilized by a

165 GTP/GDP-Pi cap. EB3 chiefly binds to the GDP-Pi rich region. During microtubule-barrier contact, reduction of microtubule

166 growth and ongoing hydrolysis are hypothesized to lead to an accelerated loss of the protective cap. **(B)** Schematic of the

167 micro-fabricated barrier with a 1.5 μm overhang made of silicon carbide (SiC). The barrier itself is composed of SiO_2 and is

168 100 nm high, forcing the growing microtubules to remain within the TIRF illumination field. Microtubules are grown from

169 stabilized GMPCPP seeds. **(C)** Scanning Electron Microscope image of two channels with barriers. The insert shows a zoom

170 of the barrier with a 1.5 μm SiC overhang. **(D)** TIRF images of the micro-fabricated channel enclosed by two barriers (white

171 dotted lines). On the left microtubules (green) are nucleated from GMPCPP-stabilized seeds (magenta) towards the barriers

172 and on the right microtubules (magenta) polymerize towards the barriers in the presence of GFP-EB3 (green). See also Fig S1

173 and Videos S1 and S2.

174

175 **Complete EB3 decay is neither needed for, nor always immediately followed by a**

176 **catastrophe**

177 The microtubule-barrier contact events leading to a stalling microtubule were analysed with

178 kymographs to obtain the contact duration and GFP-EB3 comet intensity prior and during

179 contact (Fig. 2A and S1, see Methods for details). Any contact events leading to microtubule

180 buckling or sliding along the barrier were excluded from the analysis. From the moment of

181 barrier contact, the EB3 intensity at the microtubule tip decreased until the onset of catastrophe

182 (Fig. 2B, S1D). We observed that for ~65% of all stalling events, a catastrophe occurred while

183 the EB comet was still decaying (> 10% of the EB signal remaining) (Fig 2C, right). For those

184 events, the mean comet intensity at the moment of catastrophe was 16% of the pre-contact

8

185   mean. For the remaining ~35% of stalling events we found a decay of the EB comet to a steady

186   near-zero value which did not immediately lead to catastrophe. Instead, the microtubules

187   remained in contact with the barrier for some time, even in the absence of an observable EB3

188   comet (Fig. 2C, left). Fitting the average EB decay from the moment of barrier contact with a

189   mono-exponential function, shows that the decay rate increases with EB3 concentration: 0.24

190   s^{-1}, 0.29 s^{-1}, and 0.40 s^{-1} for 20, 50, and 100 nM EB3 respectively (Fig. 2D). The presence of

191   EB3 thus accelerates the decay of the EB comet during stalling events as predicted from its

192   increasing effect on the GTP hydrolysis rate (Maurer et al., 2014; Zhang et al., 2015).

193

9
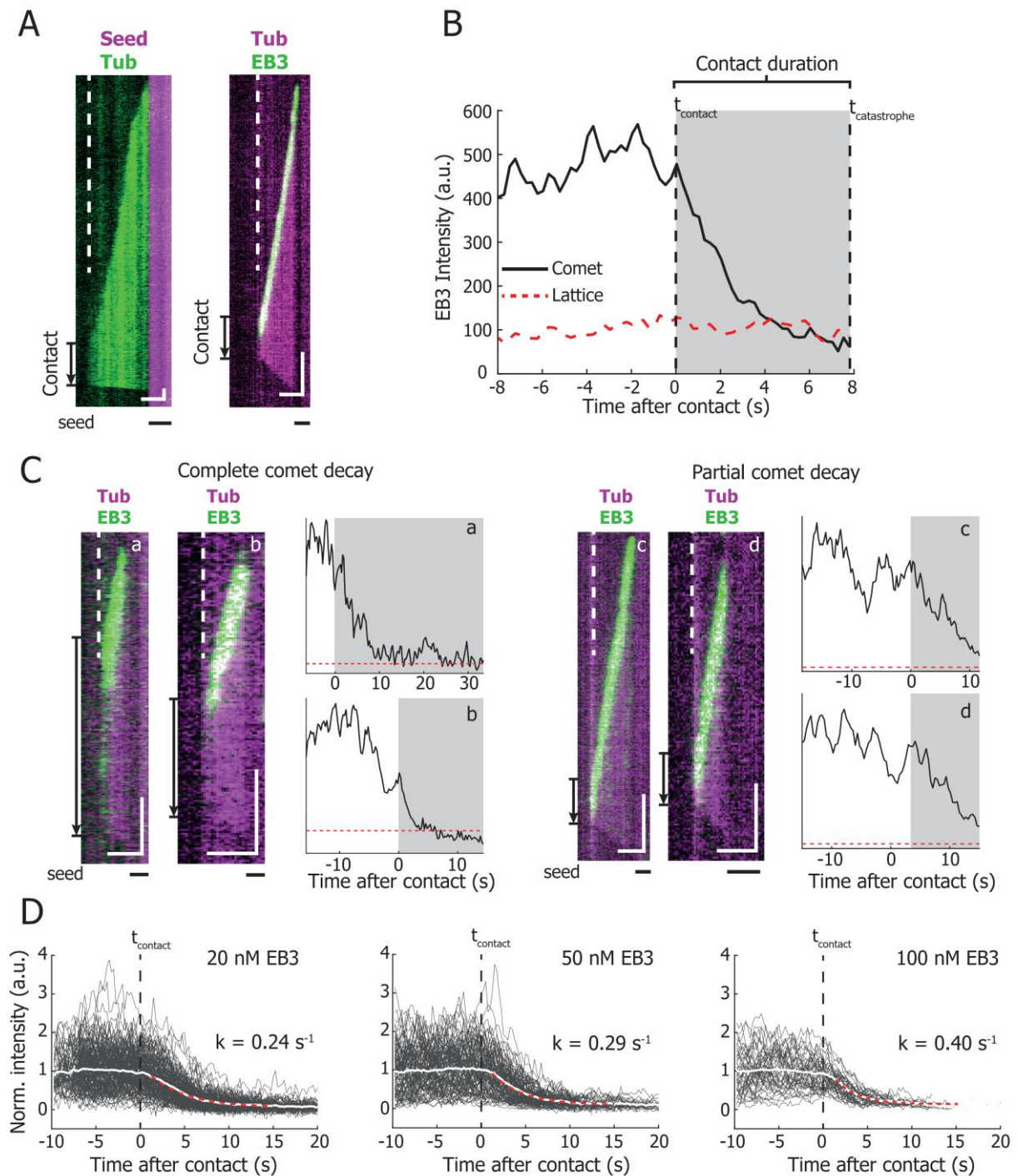
194 **Figure 2. Microtubule stalling events *in vitro*. (A)** Representative kymographs of a microtubule-barrier contact event in the
195 presence of 15 µM Hilyte488-labelled tubulin (left) and in the presence of 15 µM rhodamine-labelled tubulin with 20 nM
196 GFP-EB3 (right). The dotted line denotes the position of the SiO₂ barrier. The duration of barrier contact is indicated with an
197 arrow. Scale bars: 2 µm (horizontal) and 10 s (vertical). **(B)** Mean intensity of the EB3 comet and the EB3 signal on the
198 microtubule lattice of the kymograph on the right in **(A)**. From the moment of microtubule-barrier contact ($t_{contact}$), the EB3
199 comet signal decays to the level of the microtubule lattice, ultimately resulting in the onset of a catastrophe ($t_{catastrophe}$)
200 after 7.75 seconds. **(C)** Several examples of stalling microtubules with their respective comet intensity traces. Traces **a-b**
201 show a full comet decay during barrier contact before the onset of a catastrophe, whereas the comet in traces **c-d** only
202 partially decays. All traces were in the presence of 15 µM tubulin. Additionally, trace **a** contained 20 nM EB3, trace **b** and **c**
203 100 nM EB3, and trace **d** 50 nM EB3. Arrows and shaded regions illustrate the duration of microtubule stalling event. Scale
204 bars: 2 µm (horizontal) and 10 s (vertical). **(D)** Normalized comet intensity traces of stalling microtubules in the presence of
205 20, 50, and 100 nM EB3, aligned on the moment of barrier contact ($t_{contact}$). The mean decays were fitted with a mono-
206 exponential model and show an increasing decay rate with increasing EB3 concentrations, resulting in decay rates of 0.24 s⁻¹,
207 0.29 s⁻¹, and 0.40 s⁻¹ for 20, 50, and 100 nM respectively. Number of stalling events analysed: 20 nM, n = 151, 50 nM, n =
208 104, and 100 nM, n = 92.

209

Monte Carlo simulation of microtubule catastrophes

211 To determine whether microtubule lifetime statistics of stalling microtubules can be understood
212 solely by a single stochastic hydrolysis step combined with net stalling of noisy microtubule
213 growth, we performed minimalistic Monte Carlo simulations of both free and stalled
214 microtubule growth. Microtubules were treated as 1D filaments with subunits of 8/13 nm
215 comprising two distinct states: GTP/GDP-Pi and GDP (Fig. 3A). We decided to ignore the
216 initial transition from GTP to GDP-Pi, which was reported to be much faster than the GDP-Pi
217 to GDP transition (Kim and Rice, 2019; Maurer et al., 2014; Rickman et al., 2017). We saw
218 this justified by the fact that our key observations changed only very moderately when the first
219 transition was included explicitly, whereas omitting this transition reduced the number of model
220 parameters. Simulated microtubules grow by addition of GTP/GDP-Pi subunits which
221 subsequently undergo random hydrolysis to GDP with rate k_{hyd} (Fig. 3A). We treat
222 microtubule growth as a discrete, biased Gaussian random walk (Antal et al., 2007; Flyvbjerg
223 et al., 1996), inspired by experimental observations that revealed a substantial diffusive
224 character of the growing microtubule tip (Gardner et al., 2011a; Kerssemakers et al., 2006;
225 Rickman et al., 2017; Schek et al., 2007). Following this model, tip growth is fully characterized
226 by the experimentally measured mean growth velocity $\langle V \rangle$ and the diffusion constant D_{tip},
227 which may also result in occasional negative growth excursions (Fig. 3B). A catastrophe is
228 triggered when a stabilizing cap (L_{cap}) that results from remaining GTP/GDP-Pi subunits is
229 lost due to a negative growth excursion and/or random hydrolysis. We assume that the

10

230   nucleotide state of the tubulins at the very tip of the microtubule are the most relevant for

231   stability: a catastrophe is triggered when the number of uninterrupted GDP subunits at the very

232   tip of the microtubule is equal or greater than $N_{unstable}$ (Brun et al., 2009; Padinhateeri et al.,

233   2012), independent of how many GTP/GDP-Pi subunits remain elsewhere in the lattice (Fig

234   3CD). The length of the stabilizing cap is thus determined by the distance between the position

235   of the microtubule tip and the position along the lattice where for the first time an uninterrupted

236   sequence (or 'island') of GDP units equal or greater than the fitting parameter $N_{unstable}$ is found

237   (Fig. 3C). Depolymerization and rescues are not considered in the model. To exclude nucleation

238   kinetics from the simulated lifetimes, a microtubule is considered to grow after reaching a

239   length of 250 nm. The simulation then only requires the three fitting parameters k_{hyd}, D_{tip}, and

240   $N_{unstable}$, all of which can be verified with experimental data (see below). The experimental

241   EB3 intensity at the microtubule tip can be compared to the total number of GTP/GDP-Pi-state

242   subunits in the simulated microtubules (Fig. 3DE, bottom).

243   Microtubule stalling is simulated by introducing a fixed maximum length $L_{barrier}$ (Fig.

244   3E). Any growth excursions that would bring the microtubule length to $L > L_{barrier}$ are

245   truncated to this maximum length. Since tip fluctuations also include occasional negative

246   growth excursions (Fig. 3B), fluctuations of the tip position continue after barrier contact (Fig.

247   3E).
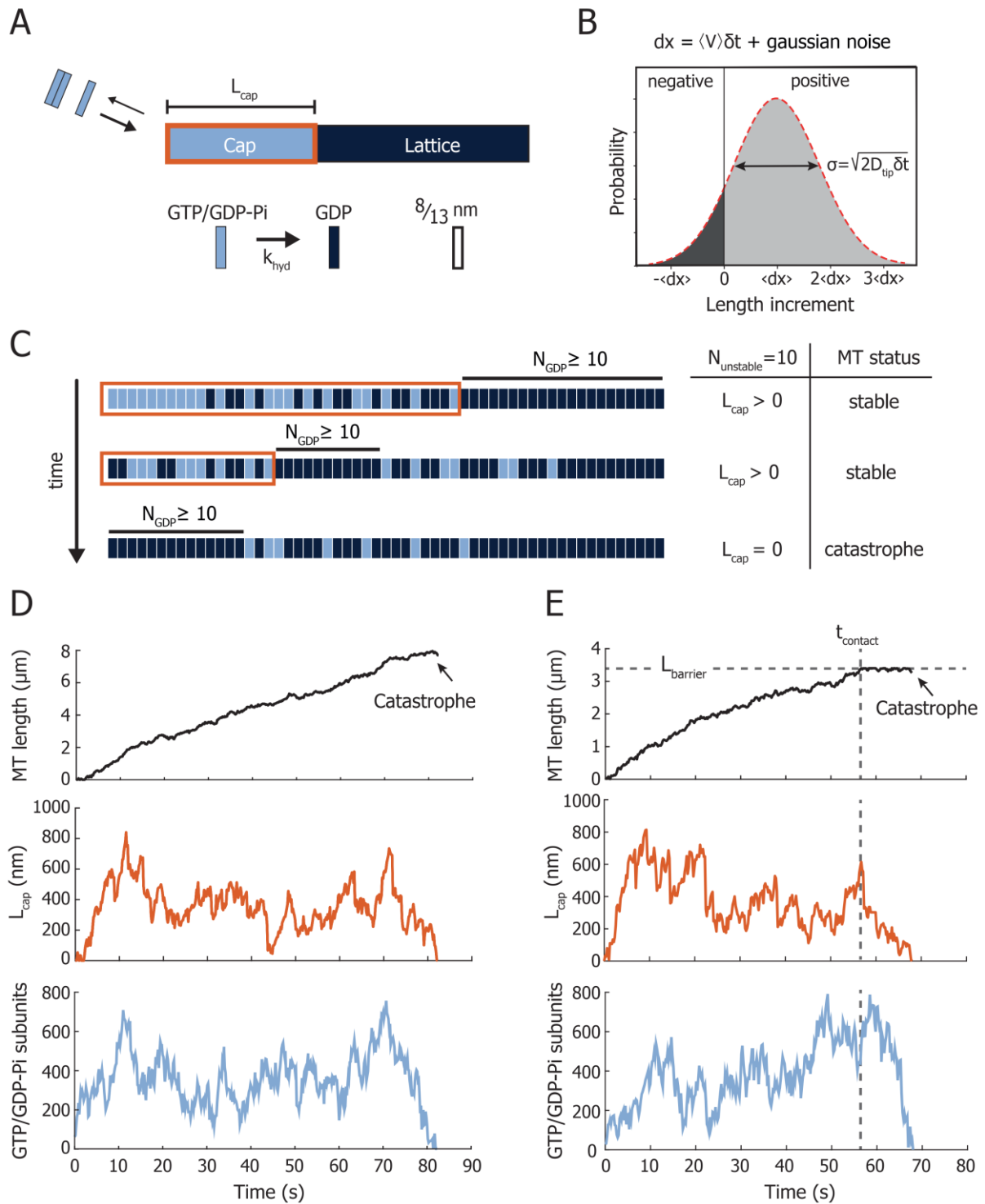
Figure 3. Monte-Carlo simulation of microtubule dynamics. **(A)** The microtubule is simulated as a one-dimensional lattice with two states, a GTP/GDP-Pi and a GDP state, that are approximately distributed in a cap with length L_{cap} and a lattice region respectively. The size of each subunit is 8/13 nm. Uncoupled stochastic hydrolysis matures the GTP/GDP-Pi-state into the GDP-state with rate k_{hyd}. **(B)** Microtubule growth is determined by a mean growth velocity $\langle V \rangle$ with added Gaussian noise characterized by D_{tip}, resulting in stochastic tip elongation following a biased random walk. The diffusive character of the tip can also produce negative growth excursions. **(C)** Detailed schematic of the nucleotide composition of the microtubule tip. The size of the stabilizing cap (orange) is defined as the region between the microtubule tip and the position along the lattice where for the first time an uninterrupted sequence of GDP subunits is equal or greater than $N_{unstable}$. A

257 catastrophe is triggered when the number of uninterrupted GDP subunits at the very tip of the microtubule is equal or greater

258 than $N_{unstable}$. As example, the case for $N_{unstable} = 10$ is shown. **(D)** Simulated microtubule growing event. **(top)** During

259 the noisy microtubule growth, the microtubule length follows a biased random walk. **(middle)** When the size of the

260 stabilizing cap (L_{cap}) is reduced to zero, i.e. when the number of uninterrupted terminal GDP subunits is equal or greater than

261 $N_{unstable}$, a catastrophe follows, and the simulation is terminated. **(bottom)** Total number of GTP/GDP-Pi subunits in the

262 simulated microtubule, which can be compared with the experimentally obtained EB3 signal. **(E)** Simulated microtubule

263 stalling event. Figures show the simulated microtubule length **(top)**, the size of the stabilizing cap (L_{cap}) **(middle)**, and the

264 total number of GTP/GDP-Pi subunits in the simulated microtubule **(bottom)**. Barrier contact is simulated by restricting the

265 maximum length of the microtubule to $L_{barrier}$. As the microtubule can undergo occasional negative growth excursions due

266 to noisy growth, the microtubule length can still fluctuate during barrier contact.

267

Obtaining the simulation parameters

269 Our 1D model relies on three fitting parameters, D_{tip}, k_{hyd}, and $N_{unstable}$. Based on existing

270 literature (Maurer et al., 2014), we expected that adding EB3 would have an effect on the

271 transition from GTP/GDP-Pi to GDP. Since EB3 also affects the microtubule growth velocity,

272 we also expected that growing microtubules may display different growth fluctuations at

273 different EB concentrations. It hence appeared reasonable to keep k_{hyd} and D_{tip} as free fitting

274 parameters, while keeping $N_{unstable}$ as a global fitting parameter that is independent of the

275 presence of EB3. We obtained values for the mean growth velocity $\langle V \rangle$ of 1.7, 2.8, 2.8, and 3.7

276 μm/min for 0, 20, 50, and 100 nM EB3 respectively and a global mean seed-barrier distance

277 $L_{barrier}$ of 3.4 μm from the experimental data.

278 To find good fitting values, we performed systematic parameter scans across a range of

279 D_{tip} and k_{hyd}, simulating 500 microtubule growth events for each parameter combination. We

280 simulated both freely growing and stalling microtubules and compared the distributions with

281 the respective experimental distributions. Using a Kolmogorov-Smirnov test as a measure of

282 the similarity between the simulated and experimental distributions, we obtained heatmaps with

283 (normalized) similarity parameters for each compared distribution (Fig. 4A). We also included

284 a comparison between the simulated GTP/GDP-Pi decay and the experimental EB decay rate

285 during stalling (Fig. 2D). The resulting range of k_{hyd} values that captured the experimental

286 decay rates was used to restrict the range of possible k_{hyd} values for the comparison of

287 simulated and experimental lifetime distributions. The parameter set best capturing all three

288 comparisons was then found by calculating the product between the heatmaps within the range

289 allowed by the decay rates (Fig. 4A and S2).
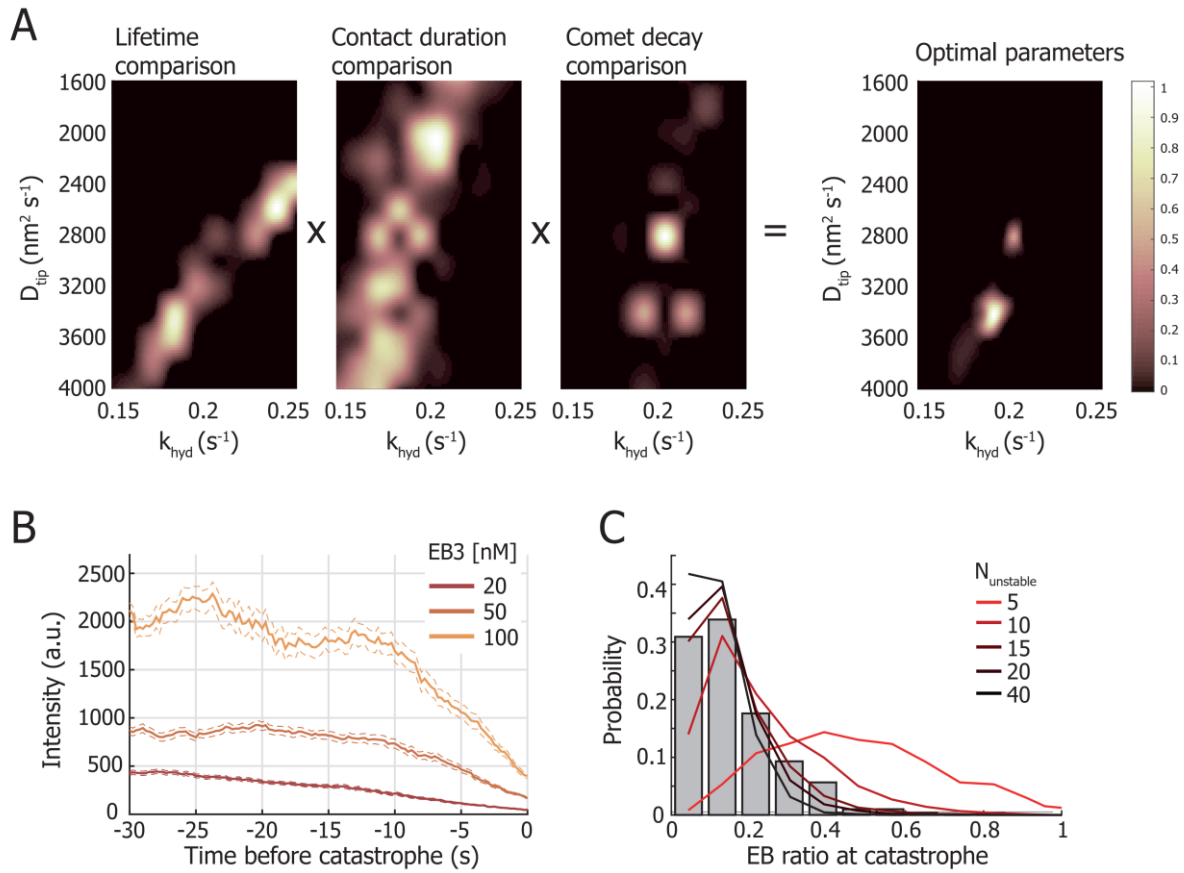
290

291 **Figure 4. Parameter determination of the 1D model. (A)** The diffusion constant D_{tip} and hydrolysis rate k_{hyd} are

292 determined by comparing the simulated microtubule lifetime distributions, the contact duration distributions, and the decay of

293 the EB signal during contact with the respective experimental distributions. The lifetime and contact duration distributions

294 are compared with the experimental distributions using a Kolmogorov-Smirnov test. A cubic interpolation of the similarity

295 values is captured in (normalized) heatmaps. The comet decay rate comparison is obtained by evaluating the absolute

296 difference between simulated rates and experimental rates. Evaluating the product of the three heatmaps results in a

297 parameter pair of D_{tip} and k_{hyd} best describing the datasets. The shown heatmaps are of 20 nM EB3. See also Fig. S2.

298 **(B)** The mean experimental EB3 signal during barrier contact, aligned on the moment of catastrophe for 20 (n=151), 50

299 (n=104), and 100 nM (n=92) EB3. The ratio between the steady-state EB3 signal prior to catastrophe (from -30 to -15

300 seconds) and at the moment of catastrophe can be compared with the simulated data. The dotted lines denote the SEM.

301 **(C)** Histogram of the ratio between the mean comet intensity during steady-state growth and the comet intensity at the

302 moment of catastrophe. The data is pooled from all experimental datasets of 20, 50, and 100 nM EB3 (n=347). The lines

303 show the simulated GTP/GDP-Pi ratio for $N_{unstable}$ values of 5, 10, 15, 20, and 40. We find that a minimum $N_{unstable}$ value

304 of 15 is required to capture the distribution of pooled experimental EB3 ratios.

305

306

307

308 **Determining the catastrophe threshold for the 1D model**

14

309   To determine the catastrophe threshold governed by $N_{unstable}$, we made use of the

310   experimentally observed decay of the mean EB signal at the barrier (Fig. 2D). Our analysis

311   yielded simultaneous fits of D_{tip} and k_{hyd} that were in very good agreement with our

312   experimental observations across a wide range of $N_{unstable}$ values. To determine an ideal value

313   for $N_{unstable}$ to match our data, we looked at the ratio between the mean EB3 signal during

314   steady-state growth and the EB3 signal at the moment of catastrophe. This would give us a

315   measure of what fraction of GTP/GDP-Pi subunits was on average hydrolysed at the moment a

316   catastrophe occurred (Fig. 4B). Higher values for $N_{unstable}$ gave rise to a longer stabilizing cap,

317   resulting in a higher ratio of hydrolysed subunits in the cap at the moment of catastrophe.

318   Comparing the combined distributions of the EB3 ratios with simulated ratios for several

319   $N_{unstable}$ values results in a minimum $N_{unstable}$ value of ~15 subunits (Fig. 4C).

320

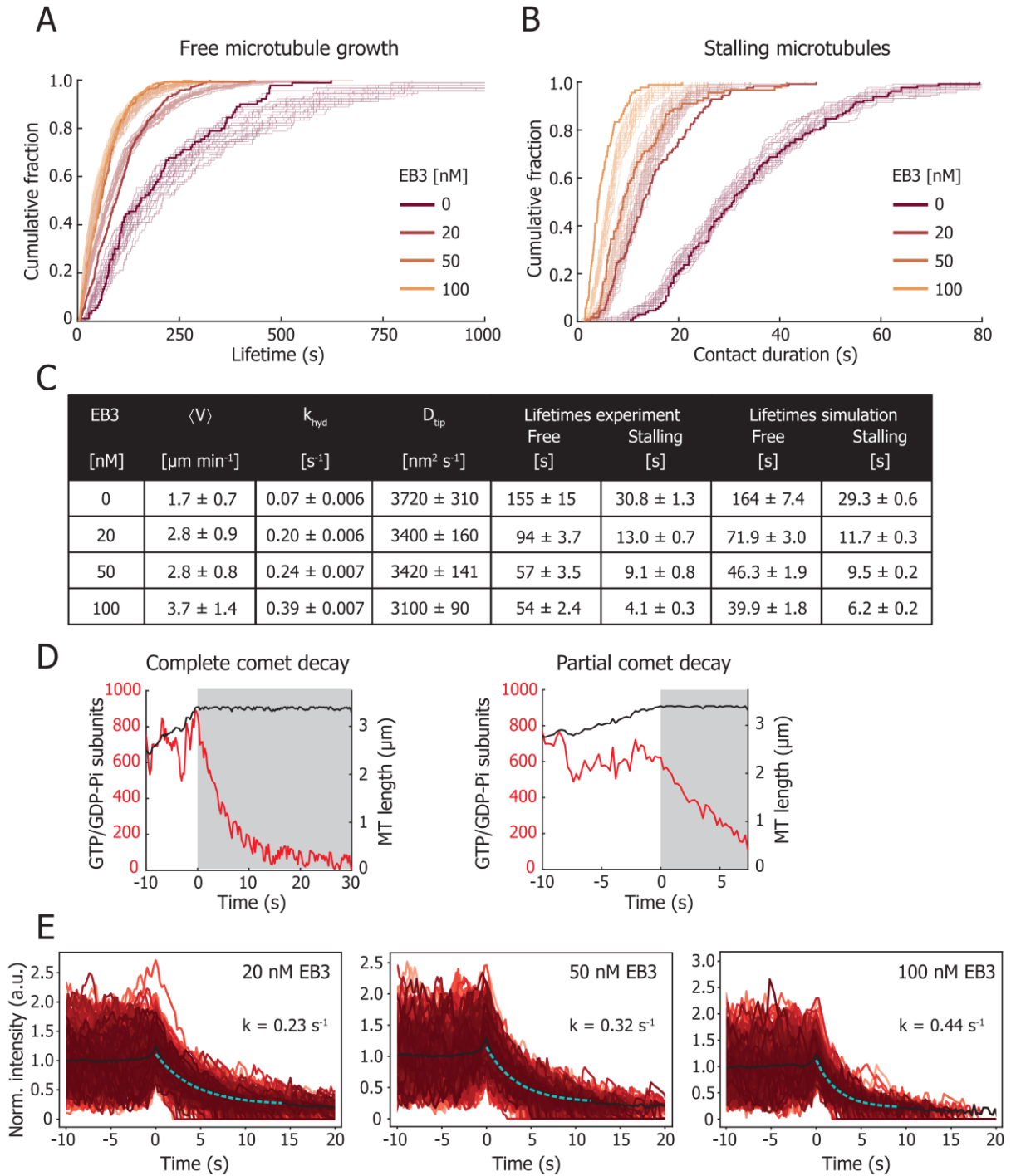321   **The 1D model can successfully capture microtubule lifetimes**

322   Figures 5A and 5B show the experimental cumulative fraction of the lifetimes of freely growing

323   microtubules and of the stalling duration respectively (bold lines), in the presence of 15 μM

324   tubulin and 0, 20, 50, and 100 nM GFP-EB3. The distribution of free lifetimes was determined

325   using microtubules growing parallel to the barriers. By bootstrapping each simulated

326   distribution obtained with the best-fitting parameters (Fig. 5C), we show 25 simulated traces

327   containing an equal number of data points as the experimental dataset (thin lines). The

328   variability in the simulated distributions provides a good visual reference of the similarity

329   between experiment and simulation (Fig. 5AB and S2). The distributions show that an

330   increasing concentration of EB3 decreases the contact duration (Fig. 5BC). In the absence of

331   EB3 the contact duration is 30.8 ± 1.3 seconds (median $\pm$ SE), whereas in the presence of 20,

332   50, and 100 nM GFP-EB3 the contact duration is reduced to respectively 13.0 ± 0.7, 9.1 ± 0.8,

333   and 4.1 ± 0.3 seconds (median $\pm$ SE). The simulated distributions capture the data well and

334   show that free microtubule lifetimes and microtubule stalling can indeed be simultaneously

335   captured with a 1D model comprising three parameters (Fig 5A-C). From the fits, we find that

336   with increasing EB3 concentration, k_{hyd} increases and D_{tip} decreases (Fig. 5C).

337   Additionally, we find both fully and partially decayed GTP/GDP-Pi intensities at the

338   moment of catastrophe, in agreement with experimentally observed event types (Fig. 5D and

339   2C). Agreement between the experimental and simulated distributions of the remaining EB3

340   signal at the moment of catastrophe was ensured with $N_{unstable} = 15$ (Fig. 4C). The mean

15

341 decay rate of GTP/GDP-Pi subunits during stalling also matches the experimental dataset well

342 and increases with increasing EB3 (Fig. 5E and 2D). The simulated barrier contact events

343 furthermore show a similar noisy comet intensity before catastrophe, confirming that the size

344 of the microtubule stabilizing cap fluctuates with time.

345

EB3	$\langle V \rangle$	k_{hyd}	D_{tip}	Lifetimes experiment		Lifetimes simulation	
				Free	Stalling	Free	Stalling
[nM]	[μm min^{-1}]	[s^{-1}]	[nm^2 s^{-1}]	[s]	[s]	[s]	[s]
0	1.7 ± 0.7	0.07 ± 0.006	3720 ± 310	155 ± 15	30.8 ± 1.3	164 ± 7.4	29.3 ± 0.6
20	2.8 ± 0.9	0.20 ± 0.006	3400 ± 160	94 ± 3.7	13.0 ± 0.7	71.9 ± 3.0	11.7 ± 0.3
50	2.8 ± 0.8	0.24 ± 0.007	3420 ± 141	57 ± 3.5	9.1 ± 0.8	46.3 ± 1.9	9.5 ± 0.2
100	3.7 ± 1.4	0.39 ± 0.007	3100 ± 90	54 ± 2.4	4.1 ± 0.3	39.9 ± 1.8	6.2 ± 0.2

346

347 **Figure 5. Free microtubule growth and microtubule stalling. (A)** The cumulative fraction of the lifetimes of freely growing

348 microtubules at increasing concentrations of 0 nM (n=90), 20 nM (n=384), 50 nM (n=262), and 100 nM (n=398) EB3. All data

16

349   were obtained with 15 μM tubulin. The bold lines show the experimental data and the thin lines show 25 bootstrapped simulated

350   distributions of equal number of datapoints as the experimental distribution. **(B)** The cumulative fraction of the microtubule-

351   barrier contact durations at increasing concentrations of 0 nM (n=131), 20 nM (n=126), 50 nM (n=90), and 100 nM (n=90)

352   GFP-EB3. All data were obtained with 15 μM tubulin. The bold lines show the experimental data and the thin lines show 25

353   bootstrapped simulated distributions of equal number of datapoints as the experimental distribution. **(C)** Table with the growth

354   velocity $\langle V \rangle$ (mean ± std), hydrolysis rate k_{hyd} (mean ± 95% CI), and diffusion constant D_{tip} (mean ± 95% CI) as determined

355   to simulate the lifetimes of freely growing microtubules and the contact duration of stalling microtubules at each EB

356   concentration (median ± SE). **(D)** Examples of simulated stalling events, showing the microtubule length and the total number

357   of GTP/GDP-Pi subunits in the lattice. The left trace shows a full comet decay during barrier contact before the onset of a

358   catastrophe, whereas the comet in traces on the right only partially decays. **(E)** Simulated decay of GTP/GDP-Pi subunits during

359   microtubule stalling at increasing EB concentration. Each dataset contains 1000 simulated events.

360

Simulation of tubulin washout

362   Recent experiments using microfluidics assisted washout of tubulin *in vitro* have shown that a

363   minimal stable cap has a length of ~10 tubulin layers at most, of which 15-30% dimers remain

364   unhydrolysed (Duellberg et al., 2016a). The observed delay between tubulin washout and

365   microtubule catastrophe is reported to be ~7 seconds (Walker et al., 1991) and shown to depend

366   on the pre-washout growth velocity (Duellberg et al., 2016a). To verify the ability of our model

367   to describe tubulin washout experiments, we simulated tubulin washout with our obtained

368   parameter set (Fig. 5C). To simulate washout, we prohibit any growth of the microtubule tip

369   after 40 seconds, but still allow microtubules to undergo negative growth excursions (Fig 3B).

370   To compare our results to published washout parameters (20 μM tubulin with 0 and 200 nM of

371   Mal3) (Duellberg et al., 2016a), we simulate tubulin washout for 15 μM tubulin in the presence

372   of 0 and 20 nM EB3, resulting in a comparable growth velocity and hydrolysis rate. The

373   difference between the concentration of Mal3 (fission yeast homolog of EB1) and EB3 required

374   to obtain a similar hydrolysis rate can be explained by the intrinsic structural differences (Roth

375   et al., 2018; von Loeffelholz et al., 2017). Our simulation of tubulin washout showed a delay

376   between washout and catastrophe of 10.2 ± 3.2 and 5.5 ± 1.8 seconds (mean ± std) for 0 and 20

377   nM EB3 (Fig. 6A), similar to the reported values of 7.3 and 3.5 seconds for 0 and 200 nM Mal3

378   (Duellberg et al., 2016a). In addition, it was reported that microtubule growth is not simply

379   paused after washout, but that microtubules slowly shrank prior to catastrophe. During the

380   simulated washout delay, we measured a slow decrease in microtubule length of 253 ± 71 nm

381   (mean ± std) for 20 nM EB3 (Fig. 6B), comparable to the reported 165 ± 105 nm for 200 nM

382   Mal3 (Duellberg et al., 2016a). Furthermore, we find that the simulated decay rate of 0.30 s^{-1}

383   (20 nM EB3) of GTP/GDP-Pi subunits from the moment of tubulin washout is in agreement

384   with the reported 0.33 s^{-1} (200 nM Mal3) (Fig. 6C).

385   Our simulated data also captures the reported positive correlation between microtubule

386   stability and growth velocity (Fig. 6D) (Duellberg et al., 2016a). The simulated washout delay

387   increases with an increasing growth velocity as measured immediately prior to washout

388   (Spearman correlation coefficient of $\rho = 0.70$). However, the correlation is lost when the

389   growth velocity is measured 10 seconds before washout ($\rho = 0.07$), in agreement with

390   published results (Duellberg et al., 2016a). We conclude that our model is thus capable of

391   accurately capturing tubulin washout experiments.

392
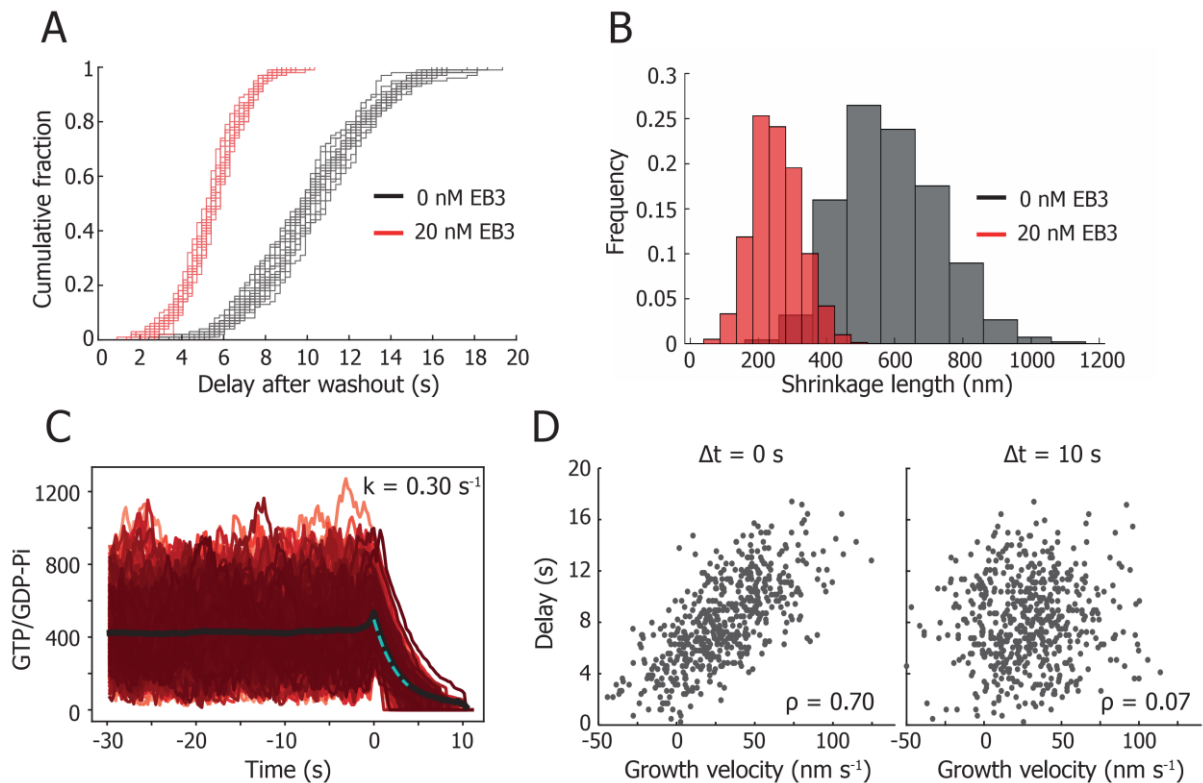
393   **Figure 6. Simulating tubulin washout. (A)** Simulation of tubulin washout following the parameters in Fig. 5C for 0 and 20

394   nM EB3. For both conditions, 25 bootstrapped distributions of 100 data points are shown. The mean delay duration between

395   washout and catastrophe is 10.3 ± 3.2 and 5.5 ± 1.8 seconds for 0 and 20 nM EB3 respectively (mean $\pm$ std). **(B)** Simulation of

396   tubulin washout following the parameters in Fig. 5C for 0 and 20 nM EB3. The mean shrinkage length of the microtubule

397   between washout and catastrophe is 588 ± 144 and 253 ± 71 nm respectively (mean $\pm$ std). **(C)** Simulation of the number of

398   GTP/GDP-Pi subunits before and during tubulin washout following the parameters in Fig. 5C for 20 nM EB3. Fitting the loss

399   of GTP/GDP-Pi subunits from the moment of washout gives a decay rate of 0.30 s^{-1}. **(D)** Scatter plot of the simulated delay

400   time dependency on the growth velocity before tubulin washout. Growth velocities measured immediately before tubulin

401   washout ($\Delta t = 0$ seconds) show a strong correlation, which is lost for growth velocities measured $\Delta t = 10$ seconds before

402   washout. The mean growth velocity is calculated from a 10 second time window. ρ is Spearman's rank correlation coefficient.

403

404   **The 1D model successfully captures the mild catastrophe dependence on microtubule**

405   **growth rates**

406   As an additional verification of our model, we simulated microtubule lifetimes and stalling

407   durations based on our previous experimental data (Fig. 7) (Janson et al., 2003). Our model can

408   simultaneously capture the reported mild reduction in catastrophe rate with increasing growth

409   velocity as well as the distribution of stalling durations (Fig. 7AB). To explain these data, we

410   had to assume a velocity-dependent tip noise (at a fixed k_{hyd} of 0.10 s^{-1}), which is in line with

411   the reported dependence of the tip noise on the growth velocity (Fig. 7C) (Gardner et al., 2011a;

412   Rickman et al., 2017). This relationship shows a linear dependence of the tip noise on the

413   growth velocity, as has been developed for a 1D model (Gardner et al., 2011a; Rickman et al.,

414   2017):

415
$$D_{tip} = \frac{a}{2}\frac{k_a + k_d}{k_a - k_d}\langle V \rangle$$

416   where a is the size of a dimer, k_a the tubulin addition rate, and k_d the tubulin dissociation rate.

417   We thus conclude that our 1D model can describe the reported mild dependence of the

418   microtubule lifetimes on the growth velocity.
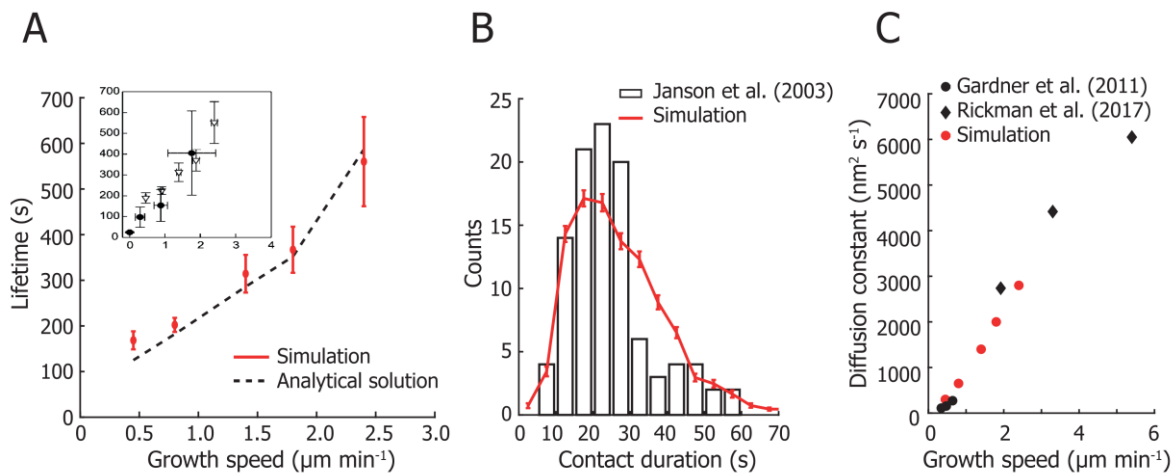
419

420   **Figure 7 Model evaluation. (A)** Simulation of microtubule lifetimes for increasing growth velocities. The simulation growth

421   velocities were obtained from (Janson et al., 2003) and combined with a global value for k_{hyd} of 0.10 s^{-1} and the determined

422   $N_{unstable}$ of 15. The insert shows the experimental lifetimes for freely growing microtubules (triangles) and for buckling

423   microtubules (dots) (Janson et al., 2003). Our simulation gives a similarly mild suppression of catastrophes with increasing

424   tubulin concentrations, with the growth velocities of 0.45, 0.8, 1.4, 1.8, and 2.4 μm min^{-1} corresponding to tubulin

425   concentrations of 7.2 (n=58), 10 (n=152), 15.2 (n=49), 20 (n=51), and 28 μM (n=30). Simulated lifetimes are given as mean ±

426   SEM with the same number of datapoints as the experimental values. The mild catastrophe suppression is also captured by the

427   analytical solution of our model (see Methods). **(B)** Histogram of the pooled stalling duration with 103 events measured at

428   15.2, 20, and 28 μM from (Janson et al., 2003) and the simulated stalling duration. The simulated values represent mean ± std

429   for n = 103 events. **(C)** The diffusion constant of the microtubule tip required to simulate the microtubule lifetimes in **(A)** based

430   on data from (Janson et al., 2003). These values agree with reported values by (Gardner et al., 2011a; Rickman et al., 2017)

431   and follow a linear dependency on the growth speed.

19

432

DISCUSSION

EB3 enhances catastrophes for stalling microtubules

Using novel micro-fabricated barriers in conjunction with TIRF microscopy, we studied the duration of barrier contact as well as the dynamics of the EB3 comet during microtubule stalling. We confirm that stalled microtubules undergo a catastrophe after 30.8 ± 1.3 seconds (median $\pm$ SE) in the absence of EB3, comparable to previously measured values (Fig. 7B) (Janson et al., 2003). The presence of EB3 further enhances catastrophes in a concentration dependent manner which results in up to five times shorter microtubule contact times at the barriers (Fig 5A-C). In earlier unpublished experiments, we made similar observations for stalling microtubules in the presence of Mal3 (Fig. S4). These shorter contact times are accompanied by an increase in the decay rate of the EB3 comet (Fig. 2D).

Additionally, we developed a simple phenomenological computational model that predicts catastrophe statistics based on parameters related to random (uncoupled) GTP hydrolysis and fluctuations in microtubule growth. Fitting the model to the data suggests that the size of the growth fluctuations (D_{tip}) decreases in the presence of EB3 (Fig. 5C). This effect would support the hypothesis that the increase in growth velocity due to the presence of EB3 is the result of a lower tubulin dissociation rate at the microtubule tip. If we assume that the tubulin association rate at the microtubule tip only depends on the soluble tubulin concentration and is therefore not affected by EB3, we would indeed expect the resulting tip noise D_{tip} to be smaller with increasing concentrations of EB3. This effect could originate from EB3 binding in between protofilaments and reducing tip fluctuations or from the hypothesis that EB3 increases the growth velocity by closing the lattice seam (Zhang et al., 2015).

455

A 1D phenomenological model successfully describes microtubule lifetimes, stalling, and tubulin washout

We developed a simple phenomenological computational model that can capture a very rich set of experimental data on dynamic microtubules. Its sole dependence on (velocity-dependent) tip noise and random hydrolysis makes it possible to build an intuition of key processes in microtubule dynamics, in particular the onset of catastrophe. We find that our model can reproduce both the experimental microtubule stalling duration and the accompanying EB comet

20

463 decay rate (Fig 5). At the same time, our model captures the reported mild reduction in
464 catastrophe rate with increasing growth velocity as well as the distribution of stalling durations
465 (Fig. 7AB). Previous 1D models were not able to describe both the mild catastrophe dependence
466 on microtubule growth rates and the size of the stabilizing cap (Brun et al., 2009; Flyvbjerg et
467 al., 1996). A reason for this was the assumption that tubulin dissociation is independent from
468 the microtubule growth velocity (Bowne-Anderson et al., 2013). This necessitated introducing
469 lateral tubulin-tubulin interactions in a 2D model to accurately capture microtubule lifetimes
470 and cap dynamics (Brun et al., 2009; Gardner et al., 2011a). Here, we showed that introducing
471 a highly dynamic tip in a 1D model is sufficient to accurately capture both the microtubule
472 lifetimes as well as the size of the stabilizing cap. The magnitude of the required simulated tip
473 noise would not be observable using fluorescence microscopy, but only with optical tweezers
474 (Gardner et al., 2011a; Kerssemakers et al., 2006; Schek et al., 2007). The extend of any
475 "blurring" of the microtubule tip due to tip noise during frame acquisition would remain below
476 the observable optical resolution (Fig. S6D).

477 We furthermore showed that our model can capture tubulin washout and reproduces a
478 similar catastrophe delay, tip shrinkage, and comet decay as previously reported (Fig. 6)
479 (Duellberg et al., 2016a). Our model also produces the same correlation between washout
480 delays and growth velocity as was recently observed experimentally (Duellberg et al., 2016a)
481 and thus captures the reported momentary nature of microtubule stability. We conclude that our
482 model can describe tubulin washout and simulate values in good agreement with experiments.

483

Microtubule stability depends on the distribution of hydrolysed dimers at the tip

485 The decay of the EB3 comet during barrier contact can provide further insights into the
486 criterium for microtubule stability. We find that microtubules can remain in a stalled state
487 without the presence of an observable EB3 comet both in our experiments and simulations
488 (compare Fig. 2C and 5D). This suggests that a stalled microtubule does not necessarily require
489 a number of GTP/GDP-Pi subunits that is large enough to be observed as a comet. The effect
490 is explained by the presence of growth fluctuations during microtubule stalling. Hydrolysed
491 subunits at the tip are continually replaced by newly incorporated unhydrolysed subunits,
492 reducing the probability of reaching the critical threshold of $N_{unstable}$ at the microtubule tip.
493 This phenomenon could also account for reported pausing events during which a microtubule

21

494   temporarily stops growing without triggering a catastrophe (VanBuren et al., 2005). It illustrates
495   that the onset of a catastrophe is not fully coupled to the presence of an observable comet.

496   To determine the stretch of hydrolysed subunits at the microtubule tip required to initiate
497   a catastrophe ($N_{unstable}$), we measured the ratio between the EB3 comet intensity at the
498   moment of catastrophe and the mean EB3 comet intensity during steady-state growth (Fig.
499   4BC). In parallel, we evaluated the decay rates of EB3 comets after initial barrier contact. Both
500   measures converge on a catastrophe threshold $N_{unstable}$ of ~15 uninterrupted hydrolysed
501   terminal subunits, which would approximate a single tubulin layer at the tip of a real 3D
502   microtubule, in line with experimental observations (Caplow and Shanks, 1996; Drechsel and
503   Kirschner, 1994). A recent finding from washout experiments showing that a microtubule
504   requires a stable cap of ~10 tubulin layers at most (Duellberg et al., 2016a) is not at odds with
505   our finding that a catastrophe is triggered when the terminal layer of tubulin is hydrolysed.
506   Because the former result is based on the average remaining density of Mal3 at the moment of
507   catastrophe after tubulin washout, it does not inform on a specific catastrophe criterium. The
508   notion that the stabilizing cap (L_{cap}) and the EB3 comet (GTP/GDP-Pi region) are large on
509   average, but that only a short stretch of hydrolysed subunits at the microtubule tip is required
510   to trigger a catastrophe, reconciles short and long cap observations (Brun et al., 2009; Duellberg
511   et al., 2016a; Molodtsov et al., 2005; Seetapun et al., 2012; Walker et al., 1991). We thus find
512   that the stability of a microtubule does not primarily depend on the size of the observed EB
513   comet, but instead on the underlying distribution of hydrolysed subunits at the microtubule tip.

514

**Both the cap size and tip fluctuations determine the onset of catastrophe**

516   To better understand the size of the stabilizing cap (L_{cap}) and its effect on the catastrophe
517   frequency, we derived an analytical expression for the position of the sequence of hydrolysed
518   subunits equal or greater than $N_{unstable}$ (see Methods for details). This position is determined
519   by $N_{unstable}$ and the underlying distribution of hydrolysed subunits. We assume that the density
520   of unhydrolysed dimers decreases exponentially along the microtubule lattice and is fully
521   characterized by k_{hyd} and $\langle V \rangle$ (Duellberg et al., 2016a; Maurer et al., 2014; Seetapun et al.,
522   2012). By treating the microtubule lattice as a series of independent Bernoulli trials, we can
523   obtain an expression for the mean position of the first occurrence of a series of hydrolysed
524   subunits equal or greater than $N_{unstable}$ (Fig. 8A and S5AB). The distance between the

525 microtubule tip and this position is equal to the size of the stabilizing cap, which means we can

526 obtain the relation between the size of the stabilizing cap and the parameters $N_{unstable}$, k_{hyd},

527 and $\langle V \rangle$ (Fig. 8BC and S5B). We find that the size of the stabilizing cap scales linearly with the

528 growth velocity $\langle V \rangle$ (Fig. 8B). The addition of EB3 however affects both the growth velocity

529 and the hydrolysis rate, the combined effect of which results in a decreasing cap size with

530 increasing EB concentration (Fig. 8C). We can calculate the mean size of the stabilizing cap in

531 our model based on k_{hyd}, $\langle V \rangle$, and $N_{unstable}$ and compare it to the length of the GTP/GDP-Pi

532 region for which the EB comet signal is a proxy. Taking $L_{comet} = \frac{\langle V \rangle}{k_{hyd}}$ as the characteristic

533 length of the EB comet (Duellberg et al., 2016a; Rickman et al., 2017), we find that the comet

534 underestimates the size of the calculated stabilizing cap (Fig 8C).

535 Having an expression for the size of the stabilizing cap, we can now explore an intuitive

536 view on how a catastrophe is triggered. The length of the cap is determined by two competing

537 processes on either end, namely noisy growth at the microtubule tip and hydrolysis in the lattice.

538 During steady-state growth, the mean length of the stabilizing cap has a constant size

539 determined by the growth velocity $\langle V \rangle$ and hydrolysis rate k_{hyd} (Duellberg et al., 2016a). We

540 observe in our simulations that catastrophes for freely growing microtubules occur as a result

541 of a short period of slowed down or negative growth (Fig 8D left and S3C), in agreement with

542 previous experimental observations (compare Fig. S3 with Fig. 7 in (Maurer et al., 2014)). This

543 shows that the onset of catastrophe is determined by the probability that growth fluctuations

544 remove the stabilizing cap. When we treat the probability for a catastrophe as the probability

545 for negative growth excursions to exceed the length of the stabilizing cap, the microtubule

546 lifetimes are successfully reproduced with the analytical solution (Fig 7A and S5D). This holds

547 true for catastrophes during free growth and after tubulin washout (Fig 8D left and middle).

548 During microtubule stalling however, continuing tip fluctuations replace hydrolysed subunits

549 at the tip for unhydrolysed subunits, reducing the effective mean hydrolysis rate. This results in

550 slowing down of the cap end and delaying the onset of catastrophe (Fig. 8D right). Additionally,

551 the longer catastrophe delay observed with microtubule stalling compared to tubulin washout

552 can be explained by the different effective tip fluctuations. After tubulin washout, loss of the

553 stabilizing cap is caused by both continued hydrolysis and the irreversible loss of tubulin

554 subunits at the tip, whereas the tip of a stalling microtubule can still recover after loss of

555 terminal subunits through tubulin addition and continue to fluctuate (Fig. 8D).

556

557
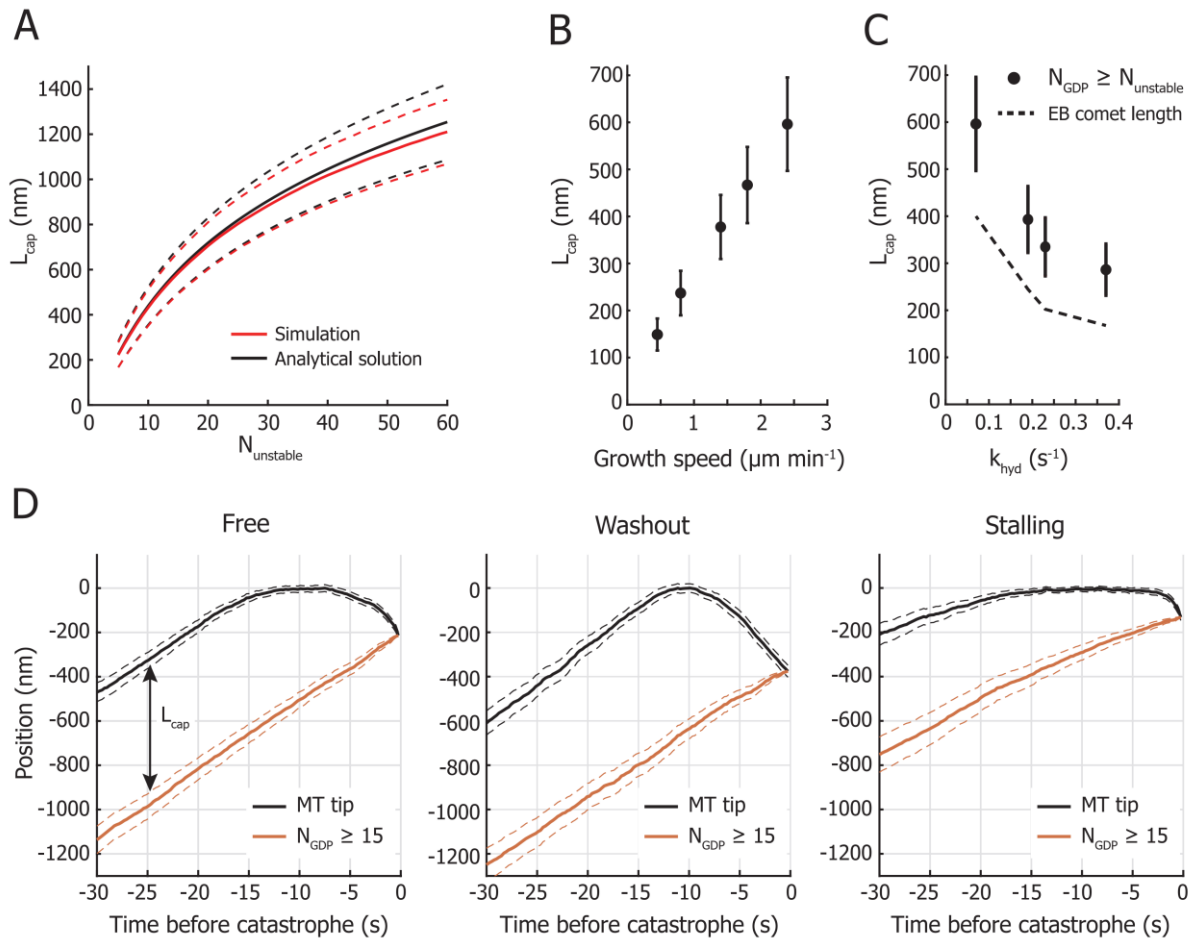
Figure 8 Fluctuations of the stabilizing cap trigger catastrophes. (A) Dependence of the cap length L_{cap} on $N_{unstable}$ (mean
± std). The simulated cap length and the numerical solution based on the analytical model are in good agreement. The shown
cap length was determined for the parameters of 0 nM EB3 in Fig. 5C. **(B)** The length of the stabilizing cap L_{cap} depends
linearly on the growth velocity $\langle V \rangle$. The cap length was calculated with the analytical model (mean ± std) and required a
constant k_{hyd} of 0.1 s^{-1} and an $N_{unstable}$ of 15, equal to the simulation parameters based on the data from (Janson et al., 2003)
(see Fig 7B). **(C)** The mean length of the stabilizing cap L_{cap} decreases with increasing hydrolysis rate k_{hyd}. The dependence
of the cap size on the hydrolysis rate is calculated with the analytical model (mean ± std) and is based on the parameters of the
EB concentrations 0, 20, 50, and 100 nM in Fig 5C. The size of the stabilizing cap based on the position of the sequence
$N_{unstable}$ is larger than the stabilizing cap based on the characteristic length of the EB signal (GTP/GDP-Pi region). **(D)**
Simulation of the position of the microtubule tip and of the position of the sequence of hydrolysed subunits defined by
$N_{unstable} = 15$ prior to catastrophe. Mean traces are for catastrophes during microtubule free growth, after tubulin washout,
and during microtubule stalling (mean ± SE). Before the onset of catastrophe, the mean cap length L_{cap} is constant during
steady-state growth as both the position of the tip and the end of the cap move with equal velocity $\langle V \rangle$. A catastrophe is triggered
when $L_{cap} = 0$, which is predominantly determined by persistent negative growth excursions of the microtubule tip. All
simulations were performed with the parameters for 0 nM EB (Fig. 5C).

Microtubule ageing is not required to describe microtubule lifetimes

24

575　An observed feature of microtubule stability lacking in our model is an age-dependent

576　catastrophe frequency. It has been reported that "younger" microtubules are more stable than

577　"older" ones (Gardner et al., 2011b; Odde et al., 1995). Ageing has also been observed through

578　a gradual reduction of the EB comet intensity during steady-state growth (Maurer et al., 2012;

579　Mohan et al., 2013) and through shorter catastrophe delays after tubulin washout for older

580　microtubules (Duellberg et al., 2016b). The two proposed processes responsible for inferring

581　ageing are either based on a multi-step lattice defect model (Bowne-Anderson et al., 2013;

582　Mohan et al., 2013) or on tapering of the microtubule tip during growth (Chretien et al., 1995;

583　Coombes et al., 2013; Duellberg et al., 2016b; VanBuren et al., 2005). Invariably, these

584　mechanisms are tightly coupled to the onset of a catastrophe and are required to understand

585　microtubule lifetimes. In our model however, we find that the onset of a catastrophe is

586　independent from microtubule ageing.

587　　Microtubule ageing is generally characterized by fitting lifetime distributions to a Gamma

588　distribution to obtain the shape parameter, a measure for the number of sequential steps required

589　to trigger a catastrophe (Gardner et al., 2011b; Odde et al., 1995). In our experimental lifetime

590　distribution, we find that the Gamma shape parameter is independent from the EB concentration

591　(Fig. S6A), in line with previous reports (Mohan et al., 2013). To account for microtubule

592　ageing in our model, we introduced time-dependent tip fluctuations (Fig. S6B). Increasing the

593　growth fluctuations with time while keeping the mean growth velocity constant, increases the

594　probability of reducing the stabilizing cap to zero due to an increase in negative growth

595　excursions. By increasing D_{tip} with a rate of 0.025 s^{-1} following a bounded exponential curve,

596　we can reproduce the experimental ageing parameters (Fig. S6C). Linking microtubule ageing

597　to an increase in tip noise and not to the hydrolysis rate or to the accumulation of defects in the

598　microtubule lattice also agrees with previous studies (Zakharov et al., 2015). It was reported

599　that microtubule ageing is in fact correlated with the frequency of encountering curled

600　protofilaments (Zakharov et al., 2015), an effect that can be represented with our

601　phenomenological description of increasing tip noise (McIntosh et al., 2018). So, although

602　microtubule ageing is not required to accurately capture microtubule lifetimes, it can be easily

603　incorporated by introducing time-dependent tip fluctuations.

604

605

606

25

Outlook

Our experimental setup will be useful for studying microtubule interactions and the functional effect of stabilizing and destabilizing microtubule associated proteins. Our approach can be used to study the influence of MAPs (Meadows et al., 2018), tubulin isotypes and PTMs (Sirajuddin et al., 2014) on the stability of pushing microtubules. Furthermore, the SiC overhangs are designed to be compatible with a previously published method to specifically functionalize the barriers with protein complexes (Taberner et al., 2014), enabling the study of microtubule end-on interactions with TIRF microscopy (Vleugel et al., 2016).

A possible extension of our 1D model to describe the effect of +TIPs on microtubule dynamics in general could be to characterize them phenomenologically by their effect on GTP hydrolysis and tip fluctuations. As the effect of EB3 can be described this way, we hypothesize that the effect of other microtubule associated proteins can be characterized similarly. To allow future extensions and modifications of our model, we have made the simulation source code available under an open-source licence on GitHub (https://github.com/florian-huber/mtdynamics) with extra documentation.

METHODS AND MATERIALS

Proteins

GFP-EB3 was a kind gift from Michel Steinmetz. All tubulin products were acquired from Cytoskeleton Inc, with all unlabelled tubulin specifically from a single lot.

Microfabrication of barriers

The fabrication method for the micro-fabricated barriers with an SiC overhang is inspired by (Kalisch et al., 2011), (Taberner et al., 2014), and (Aher et al., 2018). All fabrication steps were performed in a cleanroom environment (van Leeuwenhoek Laboratory, NanoLab NL). The barrier was designed with the following considerations in mind:

- The width of the channels should favour stalling events over buckling events, but remain large enough for GMPCPP-stabilized seeds to easily land.

- A bottom layer of SiC is needed to prevent etching into the coverslip during a Buffered Oxide Etch. This layer needs to be as thin as possible to prevent photon absorption by the semiconductor resulting in a diminished signal-to-noise and surface heating. Although SiC is transparent for wavelengths > 0.5 µm, its bandgap of ~2.8 eV can result

639   in photon absorption for the commonly used 405 and 488 nm lasers (Pham, 2004). Using
640   PE-CVD, 10 nm is thinnest layer we could fabricate while still maintaining the layer's
641   integrity to protect the coverslip from the Buffered Oxide Etch.
642 - The layer of SiO_2 of 100 nm ensures that the microtubule can polymerize underneath
643   the overhang while remaining inside the evanescent wave.
644 - The top layer of SiC is 250 nm thick to ensure mechanical stability, while still allowing
645   to observe microtubules growing on top of the barrier despite some photon absorption.
646

647 To start, glass coverslips (24x24 mm, #1) were cleaned for 10 min with base piranha, a mixture
648 of $H_2O:NH_4OH:H_2O_2$ in a 5:1:1 ratio heated to 70°C. Then, three sequential layers of SiC (10
649 nm), SiO2 (100 nm), and SiC (250 nm) are deposited on the cleaned surface via Plasma-
650 Enhanced Chemical Vapour Deposition (PE-CVD) at 300°C (Oxford Instruments PlasmaPro
651 80). PE-CVD ensures a surface smooth enough for TIRF microscopy with fast deposition rates
652 (70 nm/min for SiO_2 and 40 nm/min for SiC).

653   In order to transfer the barrier pattern to the surface, UV lithography is used. First, to
654 aid in the adhesion of the photoresist, a few drops of hexamethyldisilazane (HMDS) are spin
655 coated on the SiC surface and allowed to dry on a 115°C hotplate for 30 seconds. Then a 1.3
656 μm layer of the positive photoresist S1813 (MicroChem) is spin coated (5000rpm) on the
657 surface and pre-baked for 90 seconds on a 115°C hotplate. Exposure of the photoresist through
658 a chromium mask with a near-UV source (320-365 nm, approx. 13 mW/cm^2) transfers the
659 barrier pattern in 4 seconds (EVgroup EVG 620). Development with MF321 (MicroPosit) for
660 60 seconds removes the UV-exposed regions of the resist.

661   Next, Reactive Ion Etching (Leybold Hereaus) with a mixture of $CHF_3:O_2$ (50 sccm:2.5
662 sccm) etches through the exposed regions of the 250 nm SiC layer and into the SiO_2 layer. The
663 etch is performed at 50 μbar and at 100 W, resulting in a bias voltage of 400 V. It is important
664 to etch completely through the top SiC layer, but only partly through the SiO_2 layer, to leave
665 the bottom SiC layer intact. Any remaining photoresist after the etch is removed by sonication
666 of the sample in acetone for 10 minutes.

667   Finally, the sample is submerged in buffered hydrofluoric acid ($HF:NH_4F = 12.5:87.5\%$)
668 to selectively etch the exposed SiO_2 with a rate of approximately 200 nm/min to obtain an
669 overhang of 1.5 μm. The final barriers are 100 nm high with an overhang of 1.5 μm, enclosing
670 channels with a width of 15 μm.

671

672 ***In vitro* microtubule dynamics assay**

27

673   Reconstitution of microtubule dynamics was performed as previously described in (Bieling et
674   al., 2007; Montenegro Gouveia et al., 2010). After cleaning the barrier sample with O_2-plasma,
675   a flow channel was constructed with a cleaned glass slide and double-sided sticky tape in such
676   a way that the channel direction is perpendicular to the barriers. Then, the surface was
677   consecutively functionalized with 0.5 mg/ml PLL-PEG-biotin(20%) (SuSoS AG, Switzerland),
678   0.2 mg/ml NeutrAvidin (Invitrogen), and 0.5 mg/ml κ-casein (Sigma). All components were
679   kept in MRB80 buffer, comprised of 80mM piperazine-N,N'-bis(2-ethanesulfonic acid), 4mM
680    $MgCl_2$, and 1mM EGTA at a pH of 6.8. The reaction mixture contained 15 μM tubulin (7%
681   rhodamine labelled) in the presence of GFP-EB3 or Hilyte488 labelled tubulin in the absence
682   of GFP-EB3, supplemented with 0.5 mg/ml κ-casein, 0.15% methylcellulose, 50 mM KCl, 1
683   mM GTP, oxygen scavenger mix (4 mM DTT, 200 μg/ml catalase, 400 μg/ml glucose oxidase,
684   50mM glucose). The reaction mix is then centrifuged in an Airfuge (Beckman Coulter) at 30psi
685   for 8 minutes to remove any aggregated complexes before being introduced to the sample.
686   GMPCPP-stabilized seeds (70% unlabelled tubulin, 18% biotinylated tubulin, 12% rhodamine-
687   labelled tubulin) were introduced to the channel with the flow direction perpendicular to the
688   barriers. Flow cells were sealed with vacuum grease and imaged on a TIRF microscope at 28-
689   30°C.

690

691   **TIRF microscopy**
692   All experiments were imaged using TIRF microscopy, consisting of an Ilas^2 system (Roper
693   Scientific) on a Nikon Ti-E inverted microscope. The Ilas^2 system is a dual illuminator for
694   azimuthal spinning TIRF illumination equipped with a 150 mW 488 nm laser, a 100 mW 561
695   nm laser, and a ZT405/488/561/640rpc dichroic mirror. Simultaneous dual-acquisition was
696   performed with two Evolve 512 EMCCD camera's (Photometrics) through a 525/50 nm and a
697   609/54 emission filter, using a Nikon CFI Plan Apochromat 100XH NA1.45 TIRF oil objective.
698   Together with an additional magnifying lens, the final magnification resulted in a pixel size of
699   107 nm/pixel. The sample was heated with a custom objective heater to 28-30°C and was kept
700   in focus with the Nikon Perfect Focus system. The hardware was controlled with MetaMorph
701   7.8.8.0 (Molecular Device).

702

703   **Image treatment**
704   The image stacks obtained with TIRF microscopy were corrected prior to data analysis. First,
705   simultaneous acquisition of rhodamine-labelled tubulin and GFP-EB3 on two cameras
706   introduced a non-linear spatial offset between the two image stacks due to imperfections in the

28

707 dichroic mirror and in the alignment of the two cameras. By scanning multiple FOVs of a
708 calibration slide containing 100 nm TetraSpeck beads (ThermoFisher) and automatically
709 locating the centroids through a custom written MATLAB script, a non-linear registration
710 profile accounting for the spatial offset was calculated. The misaligned image stack was
711 corrected by applying this registration profile based on the position of ~500 bead positions.
712 Additionally, any sample drift was corrected by subpixel image registration through cross-
713 correlation (Guizar-Sicairos et al., 2008).

714 Secondly, some scattering of excitation light at the edge of the SiC overhang made
715 proper determination of the GFP-EB3 signal near the barrier difficult. Although this effect was
716 mostly mediated by creating a wide undercut that physically separated the edge of the overhang
717 from the barrier, a correction was nonetheless applied. To correct the signal, the minimum
718 intensity value of each pixel in the image stack was subtracted from that pixel in each image.
719 This correction enabled tracking of the EB3 comet near the barrier and accurate measurement
720 of the EB3 comet intensity.

721 Thirdly, a general background subtraction was performed in Fiji (Schindelin et al., 2012)
722 to correct for inhomogeneous illumination.

723

724 **Image analysis**

725 Analysis of the images was partly performed with Fiji and with MATLAB. After the image
726 treatment described above, kymographs were created by drawing straight lines of 9-pixel width
727 (0.95 µm) along growing microtubules using KymoResliceWide plugin with maximum
728 transverse intensity (http://fiji.sc/KymoResliceWide). Each growth event in the kymographs
729 was manually traced to determine the position of the microtubule tip. This position was then
730 used to fit the EB3 comet to obtain its position and intensity, using the intensity profile:

731
$$I(x) = I_A \cdot exp\left[\frac{(x-x_c)^2}{\sigma^2}\right] + I_{bkg},$$

732 where $I(x)$ is the fluorescence intensity, I_{bkg} is the background intensity, I_A is the intensity
733 amplitude, x_c is the position of the peak of the EB3 comet, and σ is the width of the EB3 comet.
734 As EB3 comet decay at the barrier makes fitting impossible, the intensity during contact was
735 determined by calculating the average intensity value in a region around the comet position and

29

736   around the barrier (Fig. S1C). The barrier contact duration and comet decay duration were

737   determined manually.

738   **Monte Carlo simulations**

739   Simulations of growing microtubules were run as a series of discrete, fixed time-steps. The

740   length of the time steps δt was chosen small enough to properly account for the random

741   hydrolysis of the subunits (P_{hyd}, the probability for a dimer to undergo hydrolysis within one

742   timestep was kept at <0.05). Further restrictions were to not exceed the desired framerate, in

743   our case the lowest used experimental frame rate of 250 ms. Due to the discrete nature of

744   microtubule growth in subunits, the next-lowest time-step for which $\langle V \rangle \delta t / L_0$ became an

745   integer was chosen, with $L_0 = \frac{8}{13} nm$ the length increment per subunit and $\langle V \rangle$ the microtubule

746   mean growth velocity.

747   Each microtubule simulation started from a few initial subunits (a 'seed') that were excluded

748   from hydrolysis, and that were not allowed to be removed during microtubule tip fluctuations.

749   Microtubule growth was simulated as a discrete, biased, Gaussian random walk. This means

750   that for each time-step δt, the microtubule length was changed by a discretized random number

751   of subunits that was drawn from a Gaussian distribution with standard deviation $\sigma = \sqrt{2D_{tip}\delta t}$

752   and centered at $\langle dx \rangle / L_0$.

753   During each time step, subunits transition from the GTP/GDP-Pi to the GDP state by random

754   hydrolysis with a rate k_{hyd}. Whenever the foremost uninterrupted strand of GDP state subunits

755   ($\geq N_{unstable}$ subunits in a row) is changed, the position of the end of the stable cap will jump

756   to the front element of this strand, which we interpret as the new position of the end of the stable

757   cap $L_{end-of-cap}$.

758   A simulation run ends when a catastrophe occurs. This happens when the stable cap shrinks to

759   zero, i.e. if $L_{tip} - L_{end-of-cap} = 0$, where L_{tip} is defined as the position of the foremost

760   subunit of the microtubule. The growth duration was defined as the time from initial growth

761   until catastrophe. To exclude nucleation kinetics from the simulated lifetimes, a microtubule is

762   considered to grow after reaching a length of 250 nm.

763   The presence of a physical barrier is modelled by introducing a fixed barrier position $L_{barrier}$.

764   Tip dynamics and random hydrolysis remained unchanged, only the microtubule length was

765   truncated whenever it would penetrate the barrier. This means the length of the microtubule

30

766   was set back to $L_{barrier}$ if $L_{tip} > L_{barrier}$. The barrier contact time was then defined as the

767   time from the microtubules first contact with the barrier until its catastrophe.

768   The simulation was written in Python 3.6 and run on standard PCs. The code to run the

769   simulation is available under an open-license on GitHub (https://github.com/florian-

770   huber/mtdynamics).

771

Analytical expression for the size of the stabilizing cap

773   The length of the stabilizing cap L_{cap} is defined as the distance between the position of the

774   microtubule tip and the first occurrence of a sequence of hydrolysed subunits N equal or greater

775   than $N_{unstable}$ (Fig. 3C). The location of this sequence of hydrolysed subunits is determined by

776   the distribution of GDP dimers in the microtubule lattice. We assume that the GTP/GDP-Pi

777   distribution at the microtubule tip decays mono-exponentially and depends on the hydrolysis

778   rate k_{hyd} and mean growth velocity $\langle V \rangle$ (Bieling et al., 2007; Duellberg et al., 2016a; Seetapun

779   et al., 2012). The probability $p(x)$ of finding a GTP/GDP-Pi subunit at position x in the lattice

780   (with the microtubule tip at $x = 0$) corresponds to

781
$$p(x) = e^{-x\frac{k_{hyd}}{\langle V \rangle}} \tag{1a}$$

782   with the probability of finding a GDP subunit at position x being

783
$$q(x) = 1 - p(x) \tag{1b}$$

784   To find the probability distribution of the position of a sequence of N sequential hydrolysed

785   dimers equal or greater than $N_{unstable}$, we treat the discrete 1D lattice as a series of independent

786   Bernoulli trials with probabilities $p(x)$ and $q(x)$ for GTP/GDP-Pi or GDP dimers respectively

787   (Fig. S5A). For a lattice shorter than N, the probability of finding a sequence of N GDP is zero

788   since the sequence is longer than the considered lattice. The probability of finding N GDP

789   subunits between the positions $x = 1$ and $x = N$ is equal to the product of the probability at

790   each position x:

791
$$P_{GDP} = \prod_{x=1}^{N} q(x) \tag{2a}$$

792   If N and $\frac{k_{hyd}}{\langle V \rangle}$ are small, the probability of finding a GDP subunit at the beginning of the

793   sequence is approximately equal to that at the end, i.e. $q(x_1) \approx q(x_N)$. Using this assumption,

794   equation $(2a)$ can be rewritten as

$$P_{GDP} = q(x)^N \qquad (2b)$$

796   For a position on the lattice further from the tip, the probability of finding a sequence

797    $N \geq N_{unstable}$ at position x, with x being the first position of the sequence, is equal to

$$P_{GDP}(x) = p(x)q(x)^N \qquad (3)$$

799   as the dimer directly preceding the sequence needs to be unhydrolyzed to initiate the sequence

800   (Fig S5A).

801   We can now obtain an expression for the probability of finding this sequence for the first time

802   at position x, by considering the probability that no sequence is found at any position closer to

803   the microtubule tip:

$$P(x|N) = 1 - \prod_{i=1}^{x-1}[1 - p(x_i)q(x_i)^N] \qquad (4)$$

805   This expression gives the cumulative distribution for finding a sequence of N GDP subunits at

806   position x during steady-state growth. We find that this approximation holds reasonably well

807   for the entire range of $N_{unstable}$ we explored using the 1D simulation (Fig. S5B). The

808   probability of finding this sequence of GDP can be captured by the Gaussian cumulative

809   distribution function:

$$P_{cap}(x) = \frac{1}{2}\left[1 + \mathrm{erf}\left(\frac{(x - L_{cap})}{\sqrt{2}\sigma_{cap}}\right)\right] \qquad (5)$$

811

812   Through numerical analysis we find that the dependency of L_{cap} on N follows a power law

813   (Fig. 8A) and can be described with

$$L_{cap}(N) = \alpha(N^\beta - 1),$$

32

815   where α and β are coefficients that depend on the hydrolysis rate and the growth velocity.

816   Similarly, we can calculate the dependence of the cap size on the parameters k_{hyd} and $\langle V \rangle$ (Fig.

817   8BC).

818

819   **Analytical expression for the catastrophe probability and microtubule lifetimes**

820   The probability for a microtubule to undergo a catastrophe within time window Δt is defined

821   as $P_{cat}(\Delta t)$ and is equal to the probability of reducing the cap size L_{cap} to zero during Δt. The

822   cap size evolves by two competing stochastic processes: it increases by dimer addition at the

823   tip and shrinks by dimer removal from the tip and hydrolysis in the lattice. To obtain an

824   analytical expression for the catastrophe probability, we consider a microtubule at steady-state

825   growth. In this frame of reference, the end of the cap is on average a constant distance from the

826   microtubule tip, as both the microtubule tip and the position of the cap end move with equal

827   velocity $\langle V \rangle$. Any fluctuations of the cap size during steady-state growth are caused by

828   fluctuations of the tip position. However, due to the stochastic nature of hydrolysis, any

829   incorporated dimers at the microtubule tip position only affect the position of the cap end after

830   a characteristic time delay τ_c, which is approximately equal to k_{hyd}^{-1} (Fig. S5C). In other

831   words, the delay gives a measure of the time window during which the fluctuations can affect

832   L_{cap}, before the position of the cap is affected by hydrolysis. The catastrophe probability is then

833   equal to the probability of tip fluctuations to exceed the position of L_{cap} during time window

834   τ_c.

835   The growth fluctuations at the microtubule tip can be described by a biased random walk with

836   Gaussian distributed steps Δx within Δt (Fig 3B).

837
$$P_{tip}(\Delta x, \Delta t) = \frac{1}{\sqrt{4\pi D_{tip}\Delta t}} \exp\left(-\frac{(\Delta x - \langle V \rangle \Delta t)^2}{4 D_{tip}\Delta t}\right) \tag{6}$$

838   Note that in the frame of reference of steady-state growth, $\langle V \rangle = 0$. To find $P_{cat}(\Delta t)$, we

839   calculate the probability that the microtubule tip exceeds L_{cap} during $\Delta t \leq \tau_c$. The survival

840   probability, the probability that the microtubule tip does not exceed L_{cap} for all times up to τ_c,

841   is defined as

842
$$S(x_c|\tau_c) \equiv \mathrm{erf}\left(\frac{x_c - x_0}{\sqrt{4\, D_{tip}\tau_c}}\right) \tag{7a}$$

33

with x_c being the critical cap-end position. Since the critical cap-end position is defined with respect to x_0 being the moving tip, we can set $x_0 = 0$ and get the probability for the tip to have reached $x \geq x_c$:

$$P_{tip}(x \geq x_c | \tau_c) = 1 - S(x_c | \tau_c) = 1 - \mathrm{erf}\left(\frac{x_c}{\sqrt{4\,D_{tip}\tau_c}}\right) \tag{7b}$$

When we set $x_c = L_{cap}$, we can calculate the catastrophe probability $P_{cat}(\tau_c)$ as the probability of the tip fluctuations exceeding the cap size L_{cap} during time window τ_c with

$$P_{cat}(\tau_c) = P_{tip}\left(x \geq L_{cap} | \tau_c\right) = 1 - \mathrm{erf}\left(\frac{L_{cap}}{\sqrt{4\,D_{tip}\tau_c}}\right) \tag{8}$$

The microtubule lifetime distribution $T_{cat}(t)$ can then be obtained by calculating the fraction of microtubules that underwent a catastrophe after each timestep τ_c (Fig. 7A and S5D):

$$T_{cat}(t) = 1 - \left(1 - P_{cat}(\tau_c)\right)^{\frac{t}{\tau_c}} \tag{9}$$

Note that the steady-state approximation becomes less accurate for large $\frac{k_{hyd}}{\langle V \rangle}$ as steady-state growth might not be reached in the first place. This leads to a lack of short events and consequently to an overestimation of the microtubule lifetimes.

Author contributions

M.K. designed and fabricated the micro-fabricated barriers, performed experiments with EB and analysed the data, developed the analytical solution, and ran simulations. F.H. developed the 1D microtubule model, wrote the simulation code and ran and analysed the simulations. SM.K. performed and analysed the experiments with Mal3. M.K, F.H., and M.D. wrote the paper. M.D. coordinated the project.

Acknowledgements

34

868 **Competing financial interests**

869 The authors declare no competing financial interests.

REFERENCES

Aher, A., M. Kok, A. Sharma, A. Rai, N. Olieric, R. Rodriguez-Garcia, E.A. Katrukha, T. Weinert, V. Olieric, L.C. Kapitein, M.O. Steinmetz, M. Dogterom, and A. Akhmanova. 2018. {CLASP} Suppresses Microtubule Catastrophes through a Single {TOG} Domain. *Dev Cell*. 46:40-58.e48, https://dx.doi.org/10.1016/j.devcel.2018.05.032

Akhmanova, A., and M.O. Steinmetz. 2015. Control of microtubule organization and dynamics: two ends in the limelight. *Nat Rev Mol Cell Biol*. 16:711-726, https://dx.doi.org/10.1038/nrm4084

Alushin, G.M., G.C. Lander, E.H. Kellogg, R. Zhang, D. Baker, and E. Nogales. 2014. High-resolution microtubule structures reveal the structural transitions in αβ-tubulin upon {GTP} hydrolysis. *Cell*. 157:1117-1129, https://dx.doi.org/10.1016/j.cell.2014.03.053

Antal, T., P.L. Krapivsky, S. Redner, M. Mailman, and B. Chakraborty. 2007. Dynamics of an idealized model of microtubule growth and catastrophe. *Phys Rev E Stat Nonlin Soft Matter Phys*. 76:041907, https://dx.doi.org/10.1103/PhysRevE.76.041907

Bayley, P., M. Schilstra, and S. Martin. 1989. A lateral cap model of microtubule dynamic instability. *FEBS Lett*. 259:181-184, https://dx.doi.org/10.1016/0014-5793(89)81523-6

Bieling, P., L. Laan, H. Schek, E.L. Munteanu, L. Sandblad, M. Dogterom, D. Brunner, and T. Surrey. 2007. Reconstitution of a microtubule plus-end tracking system in vitro. *Nature*. 450:1100-1105, https://dx.doi.org/10.1038/nature06386

Bollinger, J.A., and M.J. Stevens. 2019. Diverse balances of tubulin interactions and shape change drive and interrupt microtubule depolymerization. *Soft Matter*. 15:8137-8146, https://dx.doi.org/10.1039/c9sm01323g

Bouchet, B.P., I. Noordstra, M. van Amersfoort, E.A. Katrukha, Y.C. Ammon, N.D. Ter Hoeve, L. Hodgson, M. Dogterom, P.W. Derksen, and A. Akhmanova. 2016. Mesenchymal Cell Invasion Requires Cooperative Regulation of Persistent Microtubule Growth by {SLAIN}2 and {CLASP}1. *Dev Cell*. 39:708-723, https://dx.doi.org/10.1016/j.devcel.2016.11.009

Bowne-Anderson, H., M. Zanic, M. Kauer, and J. Howard. 2013. Microtubule dynamic instability: a new model with coupled {GTP} hydrolysis and multistep catastrophe. *Bioessays*. 35:452-461, https://dx.doi.org/10.1002/bies.201200131

Brangwynne, C.P., F.C. MacKintosh, S. Kumar, N.A. Geisse, J. Talbot, L. Mahadevan, K.K. Parker, D.E. Ingber, and D.A. Weitz. 2006. Microtubules can bear enhanced compressive loads in living cells because of lateral reinforcement. *J Cell Biol*. 173:733-741, https://dx.doi.org/10.1083/jcb.200601060

903   Brangwynne, C.P., F.C. MacKintosh, and D.A. Weitz. 2007. Force fluctuations and polymerization
904   dynamics of intracellular microtubules. *Proc Natl Acad Sci U S A*. 104:16128-16133,
905   https://dx.doi.org/10.1073/pnas.0703094104

906   Brouhard, G.J., and L.M. Rice. 2018. Microtubule dynamics: an interplay of biochemistry and
907   mechanics. *Nat Rev Mol Cell Biol*. 19:451-463, https://dx.doi.org/10.1038/s41580-018-0009-y

908   Brun, L., B. Rupp, J.J. Ward, and F. Nedelec. 2009. A theory of microtubule catastrophes and their
909   regulation.   *Proc   Natl   Acad   Sci   U   S   A*.   106:21173-21178,
910   https://dx.doi.org/10.1073/pnas.0910774106

911   Caplow, M., and J. Shanks. 1996. Evidence that a single monolayer tubulin-{GTP} cap is both necessary
912   and   sufficient   to   stabilize   microtubules.   *Mol   Biol   Cell*.   7:663-675,
913   https://dx.doi.org/10.1091/mbc.7.4.663

914   Carlier, M.F., and D. Pantaloni. 1981. Kinetic analysis of guanosine 5'-triphosphate hydrolysis
915   associated   with   tubulin   polymerization.   *Biochemistry*.   20:1918-1924,
916   http://www.ncbi.nlm.nih.gov/pubmed/7225365

917   Carlier, M.F., and D. Pantaloni. 1982. Assembly of microtubule protein: role of guanosine di- and
918   triphosphate   nucleotides.   *Biochemistry*.   21:1215-1224,
919   https://www.ncbi.nlm.nih.gov/pubmed/7074077

920   Chen, Y.D., and T.L. Hill. 1985. Monte {C}arlo study of the {GTP} cap in a five-start helix model of a
921   microtubule.   *Proc   Natl   Acad   Sci   U   S   A*.   82:1131-1135,
922   https://www.ncbi.nlm.nih.gov/pubmed/3856250

923   Chretien, D., S.D. Fuller, and E. Karsenti. 1995. Structure of growing microtubule ends: two-
924   dimensional sheets close into tubes at variable rates. *J Cell Biol*. 129:1311-1328,
925   https://dx.doi.org/10.1083/jcb.129.5.1311

926   Coletti, C., M.J. Jaroszeski, A. Pallaoro, A.M. Hoff, S. Iannotta, and S.E. Saddow. 2007. Biocompatibility
927   and wettability of crystalline {S}i{C} and {S}i surfaces. *Conf Proc IEEE Eng Med Biol Soc*.
928   2007:5850-5853, https://dx.doi.org/10.1109/IEMBS.2007.4353678

929   Colin, A., P. Singaravelu, M. Thery, L. Blanchoin, and Z. Gueroui. 2018. Actin-Network Architecture
930   Regulates Microtubule Dynamics. *Curr Biol*, https://dx.doi.org/10.1016/j.cub.2018.06.028

931   Coombes, C.E., A. Yamamoto, M.R. Kenzie, D.J. Odde, and M.K. Gardner. 2013. Evolving tip structures
932   can   explain   age-dependent   microtubule   catastrophe.   *Curr   Biol*.   23:1342-1348,
933   https://dx.doi.org/10.1016/j.cub.2013.05.059

934   Das, D., D. Das, and R. Padinhateeri. 2014. Force-induced dynamical properties of multiple cytoskeletal
935   filaments   are   distinct   from   that   of   single   filaments.   *PLoS   One*.   9:e114014,
936   https://dx.doi.org/10.1371/journal.pone.0114014

937   Debs, G.E., M. Cha, X. Liu, A.R. Huehn, and C.V. Sindelar. 2020. Dynamic and asymmetric fluctuations
938   in the microtubule wall captured by high-resolution cryoelectron microscopy. *Proc Natl Acad*
939   *Sci U S A*. 117:16976-16984, https://dx.doi.org/10.1073/pnas.2001546117

940   Dhar, S., O. Seitz, M.D. Halls, S. Choi, Y.J. Chabal, and L.C. Feldman. 2009. Chemical properties of
941   oxidized silicon carbide surfaces upon etching in hydrofluoric acid. *J Am Chem Soc*. 131:16808-
942   16813, https://dx.doi.org/10.1021/ja9053465

943   Dogterom, M., and G.H. Koenderink. 2019. Actin-microtubule crosstalk in cell biology. *Nat Rev Mol Cell*
944   *Biol*. 20:38-54, https://dx.doi.org/10.1038/s41580-018-0067-1

945   Drechsel, D.N., and M.W. Kirschner. 1994. The minimum GTP cap required to stabilize microtubules.
946   *Curr Biol*. 4:1053-1061, https://dx.doi.org/10.1016/s0960-9822(00)00243-8

947   Duellberg, C., N.I. Cade, D. Holmes, and T. Surrey. 2016a. The size of the {EB} cap determines
948   instantaneous microtubule stability. *Elife*. 5, https://dx.doi.org/10.7554/eLife.13470

949   Duellberg, C., N.I. Cade, and T. Surrey. 2016b. Microtubule aging probed by microfluidics-assisted
950   tubulin washout. *Mol Biol Cell*. 27:3563-3573, https://dx.doi.org/10.1091/mbc.E16-07-0548

951   Flyvbjerg, H., T.E. Holy, and S. Leibler. 1996. Microtubule dynamics: {C}aps, catastrophes, and coupled
952   hydrolysis. *Phys Rev E Stat Phys Plasmas Fluids Relat Interdiscip Topics*. 54:5538-5560,
953   https://www.ncbi.nlm.nih.gov/pubmed/9965740

954   Gardner, M.K., B.D. Charlebois, I.M. Janosi, J. Howard, A.J. Hunt, and D.J. Odde. 2011a. Rapid
955   microtubule self-assembly kinetics. *Cell*. 146:582-592,
956   https://dx.doi.org/10.1016/j.cell.2011.06.053

957   Gardner, M.K., M. Zanic, C. Gell, V. Bormuth, and J. Howard. 2011b. Depolymerizing kinesins {K}ip3 and
958   {MCAK} shape cellular microtubule architecture by differential control of catastrophe. *Cell*.
959   147:1092-1103, https://dx.doi.org/10.1016/j.cell.2011.10.037

960   Gregoretti, I.V., G. Margolin, M.S. Alber, and H.V. Goodson. 2006. Insights into cytoskeletal behavior
961   from computational modeling of dynamic microtubules in a cell-like environment. *J Cell Sci*.
962   119:4781-4788, https://dx.doi.org/10.1242/jcs.03240

963   Guizar-Sicairos, M., S.T. Thurman, and J.R. Fienup. 2008. Efficient subpixel image registration
964   algorithms. *Opt Lett*. 33:156-158, https://www.ncbi.nlm.nih.gov/pubmed/18197224

965   Gurel, P.S., A.L. Hatch, and H.N. Higgs. 2014. Connecting the cytoskeleton to the endoplasmic reticulum
966   and {G}olgi. *Curr Biol*. 24:R660-R672, https://dx.doi.org/10.1016/j.cub.2014.05.033

967   Janson, M.E., M.E. de Dood, and M. Dogterom. 2003. Dynamic instability of microtubules is regulated
968   by force. *J Cell Biol*. 161:1029-1034, https://dx.doi.org/10.1083/jcb.200301147

969   Kalisch, S.M., L. Laan, and M. Dogterom. 2011. Force generation by dynamic microtubules in vitro.
970   *Methods Mol Biol*. 777:147-165, https://dx.doi.org/10.1007/978-1-61779-252-6_11

971   Karr, T.L., and D.L. Purich. 1978. Examination of tubulin-nucleotide interactions by protein fluorescence
972   quenching measurements. *Biochem Biophys Res Commun*. 84:957-961,
973   https://www.ncbi.nlm.nih.gov/pubmed/728162

974   Kerssemakers, J.W., E.L. Munteanu, L. Laan, T.L. Noetzel, M.E. Janson, and M. Dogterom. 2006.
975   Assembly dynamics of microtubules at molecular resolution. *Nature*. 442:709-712,
976   https://dx.doi.org/10.1038/nature04928

977   Kim, T., and L.M. Rice. 2019. Long-range, through-lattice coupling improves predictions of microtubule
978   catastrophe. *Mol Biol Cell*. 30:1451-1462, https://dx.doi.org/10.1091/mbc.E18-10-0641

979   Komarova, Y.A., I.A. Vorobjev, and G.G. Borisy. 2002. Life cycle of {MT}s: persistent growth in the cell
980   interior, asymmetric transition frequencies and effects of the cell boundary. *J Cell Sci*.
981   115:3527-3539, https://www.ncbi.nlm.nih.gov/pubmed/12154083

982   Laan, L., J. Husson, E.L. Munteanu, J.W. Kerssemakers, and M. Dogterom. 2008. Force-generation and
983   dynamic instability of microtubule bundles. *Proc Natl Acad Sci U S A*. 105:8920-8925,
984   https://dx.doi.org/10.1073/pnas.0710311105

985   Lee, C.T., and E.M. Terentjev. 2019. Structural effects of cap, crack, and intrinsic curvature on the
986   microtubule catastrophe kinetics. *J Chem Phys*. 151:135101,
987   https://dx.doi.org/10.1063/1.5122304

988   Letort, G., F. Nedelec, L. Blanchoin, and M. Thery. 2016. Centrosome centering and decentering by
989   microtubule network rearrangement. *Mol Biol Cell*. 27:2833-2843,
990   https://dx.doi.org/10.1091/mbc.E16-06-0395

991   Margolin, G., I.V. Gregoretti, T.M. Cickovski, C. Li, W. Shi, M.S. Alber, and H.V. Goodson. 2012. The
992   mechanisms of microtubule catastrophe and rescue: implications from analysis of a dimer-
993   scale computational model. *Mol Biol Cell*. 23:642-656, https://dx.doi.org/10.1091/mbc.E11-
994   08-0688

995   Margolin, G., I.V. Gregoretti, H.V. Goodson, and M.S. Alber. 2006. Analysis of a mesoscopic stochastic
996   model of microtubule dynamic instability. *Phys Rev E Stat Nonlin Soft Matter Phys*. 74:041920,
997   https://dx.doi.org/10.1103/PhysRevE.74.041920

998   Maurer, S.P., P. Bieling, J. Cope, A. Hoenger, and T. Surrey. 2011. {GTP}γ{S} microtubules mimic the
999   growing microtubule end structure recognized by end-binding proteins ({EB}s). *Proc Natl Acad
1000   Sci U S A*. 108:3988-3993, https://dx.doi.org/10.1073/pnas.1014758108

1001   Maurer, S.P., N.I. Cade, G. Bohner, N. Gustafsson, E. Boutant, and T. Surrey. 2014. {EB}1 accelerates
1002   two conformational transitions important for microtubule maturation and dynamics. *Curr Biol*.
1003   24:372-384, https://dx.doi.org/10.1016/j.cub.2013.12.042

1004   Maurer, S.P., F.J. Fourniol, G. Bohner, C.A. Moores, and T. Surrey. 2012. {EB}s recognize a nucleotide-
1005   dependent structural cap at growing microtubule ends. *Cell*. 149:371-382,
1006   https://dx.doi.org/10.1016/j.cell.2012.02.049

1007   McIntosh, J.R., E. O'Toole, G. Morgan, J. Austin, E. Ulyanov, F. Ataullakhanov, and N. Gudimchuk. 2018.
1008   Microtubules grow by the addition of bent guanosine triphosphate tubulin to the tips of curved
1009   protofilaments. *J Cell Biol*, https://dx.doi.org/10.1083/jcb.201802138

1010   Meadows, J.C., L.J. Messin, A. Kamnev, T.C. Lancaster, M.K. Balasubramanian, R.A. Cross, and J.B.
1011   Millar. 2018. Opposing kinesin complexes queue at plus tips to ensure microtubule
1012   catastrophe at cell ends. *EMBO Rep*. 19, https://dx.doi.org/10.15252/embr.201846196

1013   Michaels, T.C., S. Feng, H. Liang, and L. Mahadevan. 2020. Mechanics and kinetics of dynamic
1014   instability. *Elife*. 9, https://dx.doi.org/10.7554/eLife.54077

1015   Mitchison, T., and M. Kirschner. 1984. Dynamic instability of microtubule growth. *Nature*. 312:237-
1016   242, http://www.ncbi.nlm.nih.gov/pubmed/6504138

1017   Mohan, R., E.A. Katrukha, H. Doodhi, I. Smal, E. Meijering, L.C. Kapitein, M.O. Steinmetz, and A.
1018   Akhmanova. 2013. End-binding proteins sensitize microtubules to the action of microtubule-
1019   targeting agents. *Proc Natl Acad Sci U S A*. 110:8900-8905,
1020   https://dx.doi.org/10.1073/pnas.1300395110

1021   Molodtsov, M.I., E.A. Ermakova, E.E. Shnol, E.L. Grishchuk, J.R. McIntosh, and F.I. Ataullakhanov. 2005.
1022   A molecular-mechanical model of the microtubule. *Biophys J*. 88:3167-3179,
1023   https://dx.doi.org/10.1529/biophysj.104.051789

1024   Montenegro Gouveia, S., K. Leslie, L.C. Kapitein, R.M. Buey, I. Grigoriev, M. Wagenbach, I. Smal, E.
1025   Meijering, C.C. Hoogenraad, L. Wordeman, M.O. Steinmetz, and A. Akhmanova. 2010. In vitro
1026   reconstitution of the functional interplay between {MCAK} and {EB}3 at microtubule plus ends.
1027   *Curr Biol*. 20:1717-1722, https://dx.doi.org/10.1016/j.cub.2010.08.020

1028   Nguyen-Ngoc, T., K. Afshar, and P. Gonczy. 2007. Coupling of cortical dynein and {G}α proteins
1029   mediates spindle positioning in {C}aenorhabditis elegans. *Nat Cell Biol*. 9:1294-1302,
1030   https://dx.doi.org/10.1038/ncb1649

1031   Nogales, E. 1999. A structural view of microtubule dynamics. *Cell Mol Life Sci*. 56:133-142,
1032   http://www.ncbi.nlm.nih.gov/pubmed/11213253

1033   Odde, D.J., L. Cassimeris, and H.M. Buettner. 1995. Kinetics of microtubule catastrophe assessed by
1034   probabilistic analysis. *Biophys J*. 69:796-802, https://dx.doi.org/10.1016/S0006-
1035   3495(95)79953-2

1036   Odde, D.J., L. Ma, A.H. Briggs, A. DeMarco, and M.W. Kirschner. 1999. Microtubule bending and
1037   breaking in living fibroblast cells. *J Cell Sci*. 112 (Pt 19):3283-3288,
1038   https://www.ncbi.nlm.nih.gov/pubmed/10504333

1039   Ohi, R., and M. Zanic. 2016. Ahead of the Curve: New Insights into Microtubule Dynamics. *F1000Res*.
1040   5, https://dx.doi.org/10.12688/f1000research.7439.1

1041   Padinhateeri, R., A.B. Kolomeisky, and D. Lacoste. 2012. Random hydrolysis controls the dynamic
1042   instability of microtubules. *Biophys J*. 102:1274-1283,
1043   https://dx.doi.org/10.1016/j.bpj.2011.12.059

1044   Pallavicini, C., A. Monastra, N.G. Bardeci, D. Wetzler, V. Levi, and L. Bruno. 2017. Characterization of
1045   microtubule buckling in living cells. *Eur Biophys J*, https://dx.doi.org/10.1007/s00249-017-
1046   1207-9

1047   Pham, H.T.M. 2004. {PE}–{CVD} {S}ilicon {C}arbide - a structured material for surface micromachined
1048   devices. *Doctoral Thesis*, https://dx.doi.org/uuid:91e396a8-5857-4e93-ba27-8a82d0d9f2b7

1049   Piedra, F.A., T. Kim, E.S. Garza, E.A. Geyer, A. Burns, X. Ye, and L.M. Rice. 2016. {GDP}-to-{GTP}
1050   exchange on the microtubule end can contribute to the frequency of catastrophe. *Mol Biol*
1051   *Cell*. 27:3515-3525, https://dx.doi.org/10.1091/mbc.E16-03-0199

1052   Preciado Lopez, M., F. Huber, I. Grigoriev, M.O. Steinmetz, A. Akhmanova, G.H. Koenderink, and M.
1053   Dogterom. 2014. Actin-microtubule coordination at growing microtubule ends. *Nat Commun*.
1054   5:4778, https://dx.doi.org/10.1038/ncomms5778

1055   Rickman, J., C. Duellberg, N.I. Cade, L.D. Griffin, and T. Surrey. 2017. Steady-state {EB} cap size
1056   fluctuations are determined by stochastic microtubule growth and maturation. *Proc Natl Acad*
1057   *Sci U S A*. 114:3427-3432, https://dx.doi.org/10.1073/pnas.1620274114

1058   Roth, D., B.P. Fitton, N.P. Chmel, N. Wasiluk, and A. Straube. 2018. Spatial positioning of {EB} family
1059   proteins at microtubule tips involves distinct nucleotide-dependent binding properties. *J Cell*
1060   *Sci*. 132, https://dx.doi.org/10.1242/jcs.219550

1061   Schek, H.T., 3rd, M.K. Gardner, J. Cheng, D.J. Odde, and A.J. Hunt. 2007. Microtubule assembly
1062   dynamics at the nanoscale. *Curr Biol*. 17:1445-1455,
1063   https://dx.doi.org/10.1016/j.cub.2007.07.011

1064   Schindelin, J., I. Arganda-Carreras, E. Frise, V. Kaynig, M. Longair, T. Pietzsch, S. Preibisch, C. Rueden,
1065   S. Saalfeld, B. Schmid, J.Y. Tinevez, D.J. White, V. Hartenstein, K. Eliceiri, P. Tomancak, and A.
1066   Cardona. 2012. Fiji: an open-source platform for biological-image analysis. *Nat Methods*.
1067   9:676-682, https://dx.doi.org/10.1038/nmeth.2019

1068   Seetapun, D., B.T. Castle, A.J. McIntyre, P.T. Tran, and D.J. Odde. 2012. Estimating the microtubule
1069   {GTP} cap size in vivo. *Curr Biol*. 22:1681-1687, https://dx.doi.org/10.1016/j.cub.2012.06.068

1070   Sirajuddin, M., L.M. Rice, and R.D. Vale. 2014. Regulation of microtubule motors by tubulin isotypes
1071   and post-translational modifications. *Nat Cell Biol*. 16:335-344,
1072   https://dx.doi.org/10.1038/ncb2920

1073   Taberner, N., G. Weber, C. You, R. Dries, J. Piehler, and M. Dogterom. 2014. Reconstituting functional
1074   microtubule-barrier interactions. *Methods Cell Biol*. 120:69-90,
1075   https://dx.doi.org/10.1016/B978-0-12-417136-7.00005-7

1076   Tilney, L.G., J. Bryan, D.J. Bush, K. Fujiwara, M.S. Mooseker, D.B. Murphy, and D.H. Snyder. 1973.
1077   Microtubules: evidence for 13 protofilaments. *J Cell Biol*. 59:267-275,
1078   https://dx.doi.org/10.1083/jcb.59.2.267

1079   Tischer, C., D. Brunner, and M. Dogterom. 2009. Force- and kinesin-8-dependent effects in the spatial
1080   regulation of fission yeast microtubule dynamics. *Mol Syst Biol*. 5:250,
1081   https://dx.doi.org/10.1038/msb.2009.5

1082   Valiyakath, J., and M. Gopalakrishnan. 2018. Polymerisation force of a rigid filament bundle: diffusive
1083   interaction leads to sublinear force-number scaling. *Sci Rep*. 8:2526,
1084   https://dx.doi.org/10.1038/s41598-018-20259-7

1085   VanBuren, V., L. Cassimeris, and D.J. Odde. 2005. Mechanochemical model of microtubule structure
1086   and self-assembly kinetics. *Biophys J*. 89:2911-2926,
1087   https://dx.doi.org/10.1529/biophysj.105.060913

1088   VanBuren, V., D.J. Odde, and L. Cassimeris. 2002. Estimates of lateral and longitudinal bond energies
1089   within the microtubule lattice. *Proc Natl Acad Sci U S A*. 99:6035-6040,
1090   https://dx.doi.org/10.1073/pnas.092504999

1091   Vleugel, M., M. Kok, and M. Dogterom. 2016. Understanding force-generating microtubule systems
1092   through in vitro reconstitution. *Cell Adh Migr*:475-494,
1093   https://dx.doi.org/10.1080/19336918.2016.1241923

1094   von Loeffelholz, O., N.A. Venables, D.R. Drummond, M. Katsuki, R. Cross, and C.A. Moores. 2017.
1095   Nucleotide- and {M}al3-dependent changes in fission yeast microtubules suggest a structural
1096   plasticity view of dynamics. *Nat Commun*. 8:2110, https://dx.doi.org/10.1038/s41467-017-
1097   02241-5

1098   Walker, R.A., N.K. Pryer, and E.D. Salmon. 1991. Dilution of individual microtubules observed in real
1099   time in vitro: evidence that cap size is small and independent of elongation rate. *J Cell Biol*.
1100   114:73-81, https://dx.doi.org/10.1083/jcb.114.1.73

1101   Waterman-Storer, C.M., J. Gregory, S.F. Parsons, and E.D. Salmon. 1995. Membrane/microtubule tip
1102   attachment complexes ({TAC}s) allow the assembly dynamics of plus ends to push and pull
1103   membranes into tubulovesicular networks in interphase {X}enopus egg extracts. *J Cell Biol*.
1104   130:1161-1169, https://dx.doi.org/10.1083/jcb.130.5.1161

1105   Zakharov, P., N. Gudimchuk, V. Voevodin, A. Tikhonravov, F.I. Ataullakhanov, and E.L. Grishchuk. 2015.
1106   Molecular and Mechanical Causes of Microtubule Catastrophe and Aging. *Biophys J*. 109:2574-
1107   2591, https://dx.doi.org/10.1016/j.bpj.2015.10.048

1108   Zhang, R., G.M. Alushin, A. Brown, and E. Nogales. 2015. Mechanistic Origin of Microtubule Dynamic

1109   Instability   and   Its   Modulation   by   {EB}   Proteins.   *Cell*.   162:849-859,

1110   https://dx.doi.org/10.1016/j.cell.2015.07.012

1111